5. SPACECRAFT ANOMALY FORECAST SYSTEM

This Chapter describes studies on forecasting of satellite anomalies in geostationary orbit based on local, non-local, and heterogeneous input data. The anomaly data are from the Meteosat-3 and Tele-X satellites. Meteosat-3 had an onboard particle monitor whereas Tele-X did not.

5.1. The geostationary plasma environment

To understand the occurrence of satellite anomalies at geostationary orbits (GEO) some basic knowledge of the plasma environment at GEO is needed. These orbits are circular at the geocentric distance of 6.6 R_E with low inclination; they are often referred to as geo-synchronous orbits although the concept of geosynchronism is a wider concept. The plasma environment is controlled by the magnetic field configuration determined by the internal dipole field and external currents in the magnetosphere and the spacecraft move through variable plasma conditions. The temporal variation of the solar wind influences the magnetosphere and the plasma characteristics at GEO. During magnetic storms the trapped particle belts inside GEO can grow in size and intensity, and more dense populations of particles (high energies) connected to the radiation belts will reach beyond the GEO and modify the spacecraft environment. The increase of particles in the radiation belts and the ring current comes mainly from the magnetosphere tail. Near and inside the GEO orbit electrons from the tail move eastward on trapped paths around the Earth whereas high-energy protons move eastward. Particles that become trapped in the Earth's nearly dipolar magnetic field form a net westward ring current.

The main contributions to the ring current are particles in the keV energy range. The radiation belts consist mainly of particles with higher energies. The particles in the inner radiation belt are in stable trapped orbits, which implies that there is no obvious entry or sink for the inner radiation belt. The source is usually assumed to be galactic or anomalous cosmic rays (GCR or ACR). Since the loss rate is low the number density can grow to significant levels. As ACRs typically are only singly- or doubly-ionised they can reach lower parts of the radiation belt and play a significant role there compared to the more numerous GCR (Klecker, 1996). The decay of the radiation belts is slow and mainly caused by pitch angle diffusion and charge exchange with neutral particles.

During quiet times the geostationary orbit is always inside the magnetopause, but during severe magnetic storms the dayside magnetopause may move inside GEO. The plasma environment a spacecraft experiences depends on the local time. Because the majority of injections occur from the tail, the morning hours usually have bursty flows of electrons. At other local times the injected particles have been smeared out to lower concentration due to the adiabatic motion, energy filter effects and particle losses at the dayside magnetopause. High-energy electrons have the highest density in the noon sector due to the adiabatic motion and the compressed dayside magnetic fields. The typical plasma sheet electron temperature at GEO distance is 1 keV but during high geomagnetic activity

the temperature can increase to 10 keV. A typical time for flux levels to build up in the magnetosphere is 80 hours (Rodgers, 1991).

The angle between the Earth's magnetic dipole axis and the rotation axis is ≈11°. The geostationary orbit is in the plane of the Earth's rotation. Since the Earth is orbiting the Sun and the Earth's rotation axis is tilted with respect to the ecliptic plane, the geostationary orbit is in the Earth-Sun plane twice a year, during the equinoxes. The rest of the year the orbit is tilted compared to the Sun-Earth line. The solar activity follows an 11-year cycle. A 27-day periodicity in magnetic storms originates from the solar rotation. The 27-day rotation can clearly be seen in the high speed solar wind streamers during the declining phase of the solar cycle.

The main charging component on the spacecraft in geostationary orbit is electrons since they are more mobile than ions (Rodgers, 1991). The geostationary orbit passes through the outer radiation belts with trapped electrons in the energy range 1 to 10 MeV. The electrons do not usually interact directly with electronic components because a modest amount of shielding (approximately 2 mm Al) is enough to stop the majority of them, although their accumulated dose can eventually cause significant component degradation. Electrons above 30 keV cause a large number of secondary particles, which in their turn can charge parts inside the spacecraft and cause deep-dielectric charging. Frederickson (1980) found that bulk charge in dielectrics required at least a week to decay and possibly much longer. Hence the effect of many bursts of energetic electrons can add up and cause problems on the spacecraft.

The time scale of charging depends on the capacitance of the surface as well as the magnitude of the charging current (Rodgers, 1991). In geostationary orbit, time scales for the charging of surfaces are in the order of seconds. The differential charging of the largest surfaces relative to each other may take from seconds to hours. Since periods of disturbed plasma likely to cause intense charging usually have time scales of minutes, equilibrium is not always reached. During eclipses, when of course photoelectron emission can not occur, the SEM-1 on Meteosat-2 frequently observed differential charging which caused potential differences of around -600 V in one hour. They disappeared minutes after the eclipse had ended. In GEO the eclipse orbits and shadowing of different surfaces are the most common cause to changes in the spacecraft potential.

5.2. Spacecraft anomaly forecasting using local environment data

5.2.1 Local environmental data

Local environmental data would always be very useful in analysis of spacecraft anomalies. The optimal case would be a scientific satellite equipped with several detectors, such as Freja discussed in the previous chapter. However, most satellites do not carry any environment monitors or just have some very simple detectors.

The USAF Defense Meteorological Satellite Program (DMSP) spacecraft carry space environmental sensors). At present the three sensors are: a space plasma monitor (SSIES-2), an auroral particle sensor (SSJ/4), and a magnetometer (SSM) (see http://www.ngdc.noaa.gov/dmsp/descriptions/dmsp_sensors.html). The data are used to make space weather spacification and forecasts at the 55th Space Weather Squadron, Falcon AFB Colorado, to determine causes of satellite malfunctions as well as to provide warnings to satellite controllers and users when hazardous environmental conditions that could adversely affect satellite operations exist. The SSJ/4 instrument is designed to measure the flux of charged particles precipitating into the atmosphere. It consists of four electrostatic analysers for the energy range 30 eV to 30 keV. The topside ionospheric plasma monitor (SSIES) measures the thermal plasma. The sensors are tailored for the sun-synchronous orbit altitude of 840 km. The SSIES, SSIES2 and SSIES3 system contain an ion retarding potential analyser, an ion drift meter, a total ion trap and a spherical electron sensor. The SSIES3 also contains a plasma plate on the ion array for measuring the ionospheric electrons. In addition to the sensors for collection environmental data the three systems contain a sensor, SENPOT, measuring the electric potential between the plasma and the spacecraft. The sensor part of SENPOT is a section of the ion sensor aperture plane, which is electrically isolated from the spacecraft by 100 Mohms. The ion sensors are Faraday cups measuring thermal ions and Langmuir probes measure thermal electrons.

The Space Test Program at the Space and Missile Center (USA) together with Phillips Laboratory Geophysics Laboratory have developed the Compact Environmental Anomaly Sensor (CEASE) to monitor the environment. The instrument is designed to provide alerts when anomalies are expected to be caused by surface charging, deep dielectric charging, SEU or radiation dose effects. The instrument stores data up to 72 hours, which can be transmitted down at request. The TSX-5 satellite is expected to be the first flight for CEASE. It is also planned for STRV-1C.

The Japanese Engineering Test Satellite-VI (ETS-VI), launched in August 1994, was equipped with a set of instruments to measure space environment effects (Goka et al., 1996a,b). The set of instruments called Technical Data Acquisition Equipment (TEDA), included a heavy ion telescope, dosimeter, magnetometer, single event upset monitor, total dose monitor, solar cell radiation damage monitor, contamination monitor, and electrostatic potential monitor.

On the Space Technology Research Vehicle (STRV-1B), launched in 1994 a Radiation Environment Monitor (REM) (Bühler et al., 1994) was flown to detect electrons and protons in a GTO orbit. REM was also flown 1994 in LEO on the space station MIR. The instrument was designed at the Paul Scherrer Institute (PSI) together with ESA. It has two Si detectors under shielding domes and detects electrons >1 MeV and protons >30 MeV (Bühler et al., 1996 a, b). The GTO passes through the most severe parts of the proton and electron radiation belts. The proton dose variation showed some variation with active solar periods, as well as a general solar-cycle-related trend. An increasing trend in proton doses was suggested to be consistent with the anti-correlation expected for protons. The electron environment was found to be very dynamic. During disturbed periods

the radiation belts correlate well with solar rotation and a clear seasonal pattern was seen. When a high-speed stream arrived, the energetic flux first showed a dropout and then an increase of the flux. For more information on REM results see, e.g., Daly (1998), Bühler et al., (1997), Bühler et al. (1998).

An improved version of REM is the Standard Radiation Environment Monitor (SREM) (Vuilleumier, 1997) which is developed and manufactured by Oerlikon-Contraves Space in co-operation with the Paul Scherrer Institute (PSI) under an ESA contract. The first SREM model is schedule for flight 1999 on STRV-1C and later on ESA satellites such as Integral and Rosetta. The instrument is calibrated with protons up to 600 MeV and electrons 5 MeV. One difference compared with the REM is that the problem with contamination of electrons in the high-energy proton channels is removed by a telescope configuration (Bühler et al., 1996a). The particle detectors measure electrons (0.3–6 MeV) and ions (8 –300 MeV) in fifteen energy bands. The instrument has two alarms for high/low dose rates, dead-time correction for alarm, detection of SEE, total radiation dosimeter, and a large memory. SREM is contained in a box with the size 10 x 12 x 22 cm, weight ≤ 2.5 kg, and power consumption < 2 W.

An integrated environmental monitoring system is developed for several commercial satellites, e.g., on Martin Marietta spacecraft (Bogorad et al., 1995) and Lockheed Martin Astrospace (Intelsat VIII/VIIIA) (Ozkul et al., 1996). The system contains two sensors, a Surface Charge Monitor consisting of a 2 x 2 inch plate, where the potential difference is measured and a Dosimeter/Internal Charge Monitor. The surface charge monitor is designed to respond to electrons with energies from 5 to 20 keV. On INTELSAT VII/VIIIA two sets of plates are included, one looking away from Earth and the other towards north or south. The dosimeter/internal charge monitor consists of radiation sensitive p-FET integrated dosimeter devices with different thickness of the shielding. The p-FET device is sensitive to electrons with energies from 200 keV to 6 MeV but does not provide particle species or energy discrimination. The main components of the dosimeters are designed, manufactured and tested at the Center for Space Microelectronics Technology, Jet Propulsion Laboratory, California Institute of Technology. The total weight of the instrument is less than 0.5 kg and the power consumption about 0.5 W.

5.2.2. Anomalies on Meteosat series satellites

The first Meteosat satellite, Meteosat-1, was launched in November 1977. The satellite was a spin-stabilised meteorological satellite with the main payload consisting of a scanning radiometer. The satellite experienced several anomalies. At the same time Meteosat-2 was being designed and the first investigation of Meteosat-1 anomalies was made already after one year (Hoge and Leverington, 1979). A clear correlation between anomalies and the spring equinox and a weaker correlation with the autumn equinox were seen for four different satellites: Skynet, Meteosat-1, Symphonies-A and B. Correlation with local time, solar direction, or eclipses could not be established. A clear correlation between anomalies on Meteosat-1 and the geomagnetic indices two days before the detected anomaly was seen. The two day delay was also indicated in the Skynet data. A ground test of

the engineering model was set up for investigation of the space environmental effects on Meteosat-1.

On Meteosat-1 about 80% of the outer surface of the satellite was not conductive, e.g., solar cell cover glass, second surface mirrors, and black paint. Large metallic surfaces of the thermal shields were not grounded because no cost-effective solution existed at that time. The grounding was a multipoint grounding system. Current injection tests did not give any failures during a five-week test period. Thermal shield test of irradiation was performed but the discharges were smaller than expected and seemed to have no impact on the satellite. The result from an electron irradiation test (Hoge and Leverington, 1979; Hoge, 1980; and Hoge, 1982) showed that virtually all isolated surfaces on Meteosat were subject to arc discharges every second or so but the energy was too low to cause any damage on-board. The test was set up to simulate typical substorm conditions.

The Meteosat-1 spacecraft charging investigation led to the recommendation for Meteosat-2 to ground the shield, to improve some critical interfaces, and to incorporate charging monitors. The charging monitors on Meteosat-2 consisted of an electron analyzer, SSJ3, built at Emmanuel College, Boston, USA, and an electrostatic discharge monitor EEM-1 built at ESA/ESTEC. The SSJ3 had an energy range of 50 eV – 20 keV in a low and a high energy channel

The Meteosat-2, with the improved design, was launched in June 1981. Meteosat-2 also encountered anomalous status changes (Hoge, 1982). During the first year a clear correlation of Meteosat-2 flux measurements and the Marecs-A satellite anomalies was seen. Most of the Marecs-A anomalies occurred when the spacecraft passed through the plasma sheet. The monitors onboard Meteosat-2 confirmed that the presence of spacecraft charging did not perturb the Meteosat-2 functions, and therefore the interest of looking at more energetic radiation was raised. From the Meteosat-2 satellite the rapid degradation of the solar array indicated the presence of high energy particles but it did not correlate with the anomalies. Coates et al. (1991) studied almost six years of anomaly data from Meteosat-2 and found that the anomalies did not fit the pattern for surface charging effects. They suggested deep-dielectric charging as the most likely explanation.

Hoge (1982) concluded that the improvements of the design of Meteosat-2 were effective although the monitored data did not agree with the hypothesis for the charging mechanism which was used to introduce these modifications. Other types of environmental effects or onboard generated interference may have been the cause of the remaining Meteosat-2 arcing anomalies. A spectrum of monitors for future launches was recommended. For Meteosat-3 a new environmental monitoring instrument SEM-2 was used to measure higher energies. The SEM-2 was built at the Mullard Space Science Laboratory, UK under an ESA/ESTEC contract.

An assessment study (Frezet et al., 1989) was made on GEO satellites, one of which was Meteosat-2. It used the NASCAP and MATCHG codes to investigate electrostatic charging, especially for the radiometer cavity on Meteosat-2. Due to the seasonal dependence the code was run for different solar aspect angles. The simulation lasted 15 minutes. Less charging was found at solstice conditions than at equinoxes because of the larger sunlit area. The study recommended avoiding floating metalisation and high-resis-

tivity material. The differential charging was reduced considerably when all conductors were grounded. Further improvements were seen when insulation black paint was made conductive and the Teflon was replaced by the lower-resistivity Kapton. With this the charging of the cavity was almost removed. In the result of the test a seasonal dependence was observed but a good correlation between severe plasma events and the observed Meteosat anomalies was lacking. This indicated that at least part of the problem was caused by "deep-dielectric charging" induced by high-energy electrons.

5.2.3. Meteosat-3 anomalies

Meteosat-3 was launched on 15 June 1988, to become one of ESA's geostationary satellites in the meteorological satellite series. The satellite was operated by Eumetsat and was moved several times (see Table 5.1).

From	To	Position
Launch 15 June 1988	June 1989	0°E
June 1989	January 1990	50°W
January 1990	April 1990	0°E
April 1990	November 1990	5°W
July 1991		50°W
late 1992		75°W
April 1993		72.8°W
February 1995	November 1995	70°W, inclined

Table 5.1. Meteosat 3 position

The anomaly set covers the time period from 21 June 1988 to 20 October 1995. The environment monitor SEM-2 was operated during the same time period except for a few months. Meteosat-3 had several types of anomalies. In Table 5.2 the anomalies are presented in 18 different categories. Most anomalies were related to the radiometer, about 70% of all anomalies. The total number of anomalies during the operational lifetime was 724.

In Figure 5.1 all anomalies from Meteosat-3 are plotted versus the local time and time of year. It shows that more anomalies occurred in the late evening/early morning sector (00-09 LT) than during the rest of the day. This has also been seen in earlier studies (Rodgers, 1991; Wilkinson, 1994; Vampola, 1994; Wrenn and Sims, 1993). The increase of anomalies is usually attributed to the injection and drift of electrons into this local time sector.

The radiometer anomalies have a peak in the midnight–morning sector (Figure 5.2), but most other anomalies are spread evenly in local time. This and earlier results (Grystad, 1997) suggest that the radiometer anomalies may have a different cause. The battery charger anomalies are clearly correlated with equinox. The image line anomalies occur late in the mission and could be due to aging or be more susceptible to cosmic rays. The rest of the anomalies are evenly spread over the year and local times. The effect of the special conditions during equinox is clear on most types of anomalies.

Code	Description	Count
1	Radiometer stops	295
2	Radiometer position jump	84
3	Radiometer position jump and stop	127
4	Other radiometer anomalies	3
5	Battery charger 1 anomaly	7
6	Battery charger 2 anomaly	49
7	Battery charger 1 and/or 2 off	14
8	Battery charger rate anomaly	4
9	Digital multiplexer 1 off / 2 on	8
10	Corrupted/lost image lines	67
11	Command decoder anomaly	3
12	Temperature reading anomaly	14
13	SIC anomaly	29
14	EDA bias jump, SIC lid jump, rad gain	5
15	VIS 2 gain jump	2
16	Regulator loop voltage anomaly	2
17	Spurious memory reconfiguration	2
18	Other anomalies	9

Table 5.2. The codes of Meteosat-3 anomalies

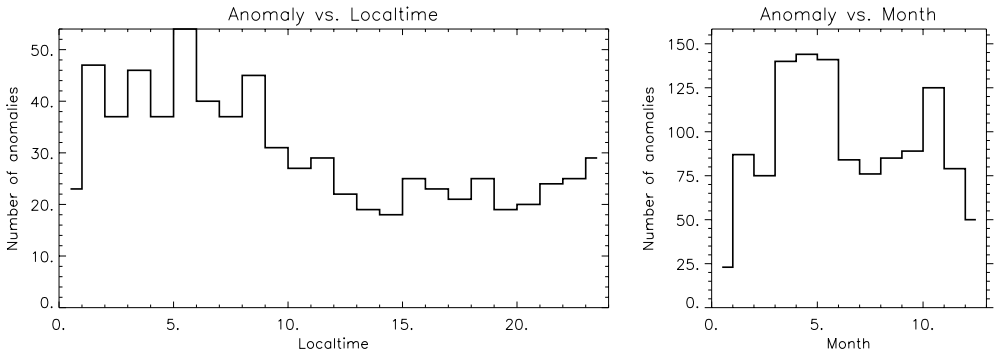

Fig 5.1. Meteosat-3 anomalies vs. the local time and month, respectively.

The solar cycle dependence (Figure 5.3) has to be carefully analysed because the operational period of the satellite covered less than one solar cycle, starting during solar maximum (1989) and continued into solar minimum. Ageing effects can make the spacecraft more susceptible to the environment. If the effect is mainly due to solar activity causing variation of plasma characteristics in the magnetosphere, the number of anomalies would be highest at the beginning of the mission. The effects solar proton events or GCRs and ACRs should give a different solar cycle dependence with more events during solar minimum. The ageing of the spacecraft is expected to increase the number of anomalies with time, although for some cases the ageing can cause anomalies to disappear. In this study we cannot separate the ageing effect from the solar cycle effect.

(a)

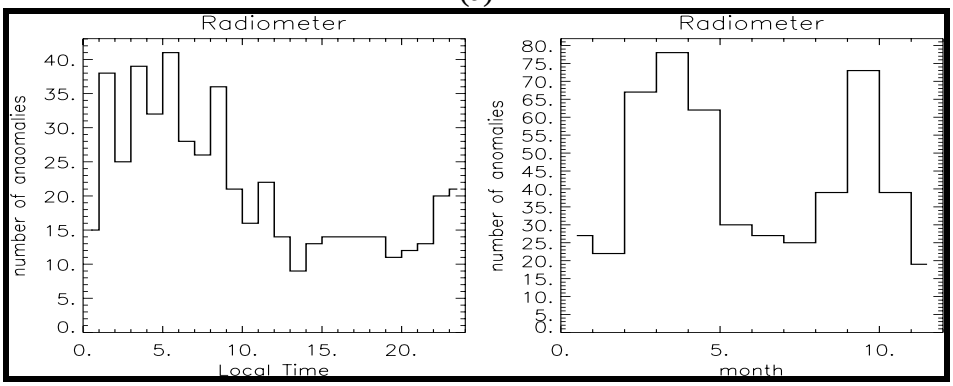

(b)

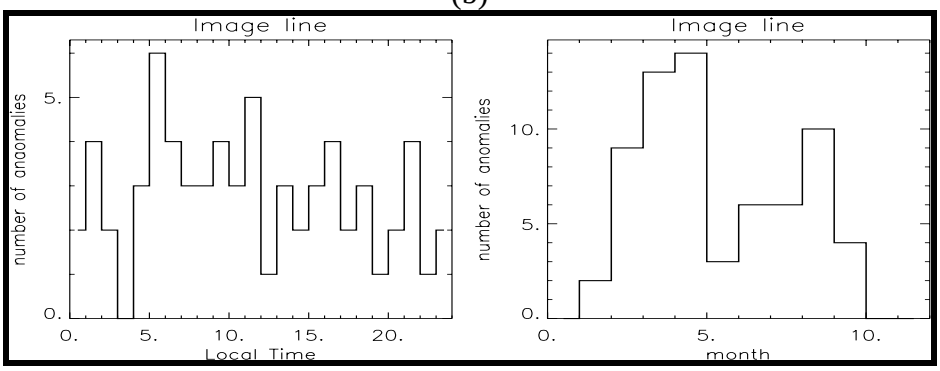

(c)

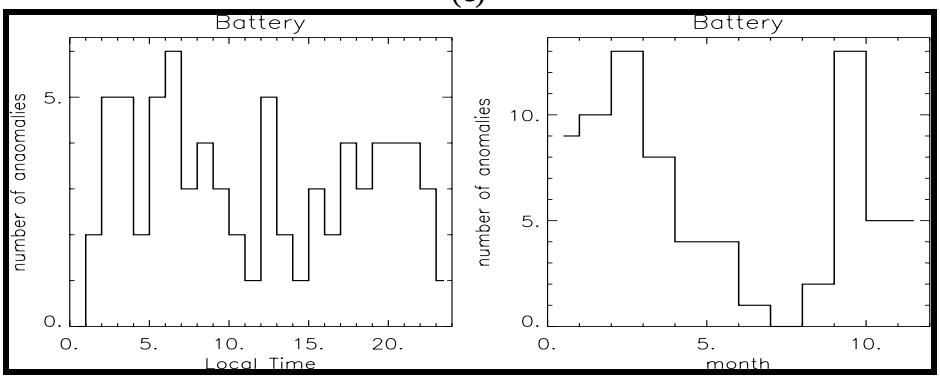

Figure 5.2. Different anomalies plotted vs. local time and month. The different figures show; a) Radiometer anomalies (code 1, 2, 3, 4) ;b) Image line anomalies (code 10) and; c) Battery anomalies (code 5, 6, 7, 8). The codes refer to Tabel 5.2.

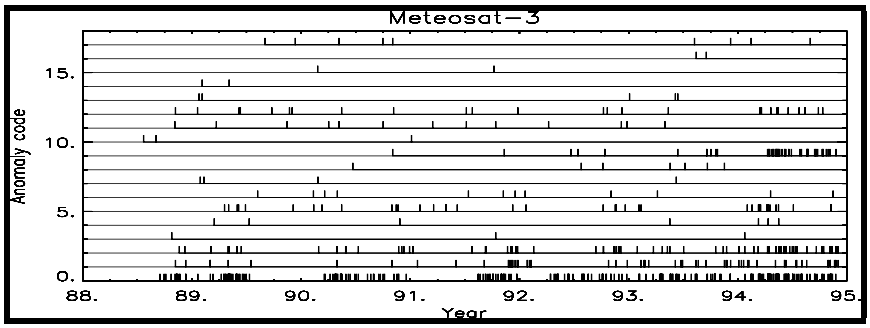

Figure 5.3. The different anomalies as function of time.

5.2.4. Earlier studies on Meteosat-3 anomalies

Rodgers (1991) studied 166 anomalies of the Meteosat-3 (also called Meteosat P2) from the radiometer together with primarily the low-resolution data from SEM-2. A clear correlation was seen between some of the anomalies and the electron flux. A statistical study showed that for a typical anomaly the flux levels had been built up during the preceding 80 hours. Anomalies correlated with the highest flux occurrence mainly at 3-9 local time (LT). Anomalies correlating with low fluxes and longer build-up times occur at 15-24 LT. Both seem to be more correlated with the high energy range on SEM-2 and indicate that deep-dielectric charging is the most likely cause. Different energy ranges and their relative importance were compared using a time window around the anomaly and an average level (not time dependent). No correlation was found with incident angle for low-resolution data but for high resolution some dependency of theta was discovered. Earlier studies showed that anomalies have a strong seasonal dependence. This suggested that eclipse periods are important. The equinox coincides with the sun shining directly into the radiometer cavity, and this should reduce the surface charging effect but would not effect the deep-dielectric charging effect. Rodgers (1991) concluded that the anomalies might have different causes but are probably due to deep-dielectric charging. The morning anomalies seemed to be triggered by a high flux of particles while evening anomalies had a long accumulation phase, over 8 days without a peak in the fluxes.

Rodgers et al. (1997) continued the study of Meteosat anomalies with the full seven-year anomaly data set (total 725 anomalies) together with the SEM-2 data. The detailed investigation was only on the radiometer anomalies (486 anomalies). They found that the highest energy channel was correlated with anomalies with high fluxes at the time of the anomaly. The 5-9 LT anomalies are mostly correlated with the high-energy channel. These were again suggested to result from deep-dielectric charging, and 16 of 121 anomalies in 5-9 LT occurred in the same 3-hour bin as the previous anomaly. The other, especially 17-21 LT, anomalies occurred after long build-up times and with relatively low fluxes at the time of the anomaly.

López Honrubia and Hilgers (1997) ivestigated pattern classification techniques for Meteosat anomaly data analysis. They used 40 anomalies over 5 years from Meteosat-3, 4, and 5 (they are known as the Meteosat P2, launched 1988, the Meteosat Operational Satellites MOP-1, mid 1989, and MOP-2, February 1994, respectively) together with high energy (>2 MeV) electron measurements from the US series of Geostationary Operational Environmental Satellites (GOES). The data set was divided into two classes “anomaly”- “non-anomaly”. The analysis was made with a Learning Vector Quantization (LVQ) network. The data set contained 2000 input vectors, 40 of which were associated with anomaly days. The input data consisted of an N-day window with N days of the mean daily flux; the window did not use information from the same day as the anomaly to make the analysis to be a forecast. The output was 1 if there was an anomaly the following day, -1 if there was an anomaly within the window N before or after and otherwise 0 (the cases with -1 were not analysed). Although limited by the small amount

of anomaly data, the technique gave evidence for correlation of this type anomaly with MeV electron data measured by GOES and for time dependent effects.

Grystad (1997) applied a similar technique as López Honrubia and Hilgers (1997) to analuse the same data as Rogers et al. (1997). Both a Bayesian linear classifier and an LVQ were used on the Meteosat -3 anomaly set and on the on-board SEM-2 instrument. The highest energy channels showed slightly different characteristics with a maximum at 4 days. The main conclusions, although still preliminary, were that the lower energy range correlates when only average flux over the latest day is considered, while for higher energies the best window length is longer.

5.2.5. Forecasting Meteosat-3 anomalies using neural networks and local data

The space environment monitor on Meteosat-3, SEM-2, covered the energy range 42.9–300 keV with the time resolution 8–10 minutes (Rodgers, 1991) The SEM-2 has a low mass (2.5 kg), power (1.8 W), and telemetry rate (1.9 bits/s). It is a solid-state detector which uses the stop length to estimate the energy. The highest energy bin includes all high-energy particles, also those which do not stop in the detector (energies above 300 keV). The energy range was selected to look for deep-dielectric charging effects. It was based on an array of five surface barrier detector-collimator systems and was built by the Los Alamos National Laboratory and calibrated by the Mullard Space Science Laboratory. The detectors were arranged in a fan shape with each detector at a different angle to the spacecraft spin axis to give five polar angle bins. The field of view of each detector was 5 degrees. Azimuthal information was obtained by the spacecraft spin. The spin axis was aligned with the Earth's north-south axis.

An anisotropy index was derived from a two-dimensional array of fluxes at each polar and azimuthal angle, summed over all energy bins. This index is calculated by fitting spherical harmonics to the data (Rodgers, 1991 and references therein). Zero second-order anisotropy index corresponds to an isotropic distribution. Negative index corresponds to an equatorially enhanced or “pancake” distribution which is frequently seen near local midnight. Most electrons in this energy range have come from the tail in this sector. The axis of symmetry of the distribution is found in the same fitting process and is expressed in terms of its polar (θ) and azimuthal angle (ϕ). Since the electrons are expected to be controlled by the magnetic field, the axis of symmetry is an indicator of the magnetic field direction although the sign and strength of the magnetic field are unknown.

The data files were stored in two sets with the resolution 8–10 min and 30 min, respectively. Only the 30 minute resolution data were used. The archive SEM-2 data files contain: flux (summed over ϕ and θ) as function of energy, flux (summed over energy and ϕ) as function of θ, flux (summed over energy and θ) as function of ϕ, flux (summed over energy) as function of ϕ and θ, total flux (summed over energy), spectral index (γ), second-order anisotropy index α, and the polar (θ) and azimuthal (ϕ) angles defining the axis of symmetry, Kp (the planetary magnetospheric activity index) and the status of the on-board memory SEU monitor.

At the beginning of the mission there were more sporadic electron fluxes (solar maximum), while at the end (solar minimum) more regular changes took place corresponding to the 27-day rotation of the Sun. There was a variation between the daily average fluxes but no clear changes of the mean flux between solar minimum and maximum. The variation during one day was larger than the day-to-day variation.

5.2.6. Anomaly data set

About 724 anomalies occurred during the almost 7 year mission of Meteosat-3. The anomalies often occurred after a period of high electron fluxes. The difference between a time period preceding a non-anomaly and a period preceding an anomaly was less than the normal daily variation (one orbit) of the electron fluxes.

A data set containing electron fluxes with a time resolution of two hours was created. During the lifetime of the Meteosat-3 satellite there were six longer (≥ 1) periods when SEM-2 was not operated. This implies that the data set has to be treated as seven separate time series. A few small gaps (≤ 4) were replaced with a linear integration from the surrounding points. The total number of two-hour-data are approximately 27500.

The forecast is based on electron fluxes as input to a neural network. The network predicts if an anomaly will occur or not (output). The desired output was set to zero (0) if no anomaly occurred within a time window and to one (1) if an anomaly occurred. The time window is selected to give a warning to a spacecraft operator as early as possible without giving too many false alarms.

Statistically, one anomaly occurred every fifth day. Therefore the time window was set to predict anomalies within 24 hours. Since the data set has a resolution of two hours this leads to one anomaly giving 12 rows of warnings in the data file. If two anomalies occur within 24 hours the number of warnings (rows with value 1) will be less than 24. Consequently, the forecast success for warnings and anomalies can be different. The total number of warnings is approximately 5200, i.e. for 19% of the total number of 2-hour-steps.

The two-hour time-series is created to keep as much information as possible from the SEM-2 measurements. For each of the five energy bins four flux values are calculated and saved in a file; the 2 hour mean flux, the maximum flux during the 2 hours, the minimum flux during the 2 hours, and an average flux from the previous 72 hours (3 days). 72 hours was selected because it is longer than a day (to average out daily variations) and less than the 80 hours of some magnetospheric storm effects. Three files with different data combinations were produced, one using all five energy bins plus information of the spectral shape (spectral index, anisotropy index, θ and ϕ), giving 24 columns for each 2-hour step (data combination called "_all"). The other combinations used only the three highest energies or the three lowest energies, giving 12 columns for each 2-hour step (called "_high" and "_low"). All data combinations contain the logarithm of the flux to make the data set more linear.

In order to limit the number of dimensions (inputs), a principal component analysis (PCA) was performed on all three data combinations creating new data sets containing

only three dimensions. The PCA gives the eigenvalues for the data set and selects the largest as the first component, the second largest variance as the second component, etc. If only the three largest components are used this will be a transformation from 24 dimensions (the data combination _all) down to three. In this case the first principal component was associated with the average, minimum, and maximum flux for all energy bins. The second principal component was associated with the running mean for all energy bins, and the third component is more of a mixture.

The data combination files (_all, _low, and _high) now contain three columns with information on the fluxes for each time step (row). In order to predict anomalies with a neural network, an input file is built with information on the magnitude of the components and the dynamics of the electron fluxes preceding the forecast. The preceding time of the forecast is selected to be a window, with a time length up to several days. If all data (with 2 hour resolution) for a selected time window are used to predict the anomaly there will be a large number of inputs. Table 5.4 shows some of the data combinations. For the combination pa3, the magnitudes at the time of the forecast are used together with the values 12 points before (i.e., 24 hours before) plus the values 24 points before. This leads to a time window of 48 hours containing three points each with 3 components, thus 9 inputs.

ref. name	point resolution	number of PCA used	total number of columns	length of time window (h)	
pa2	3	3	9	24	
pa3	12	3	9	48	
pa4	3+12	6	18	48	points at 0, 4, 7, 10, 12, and 48
pa5	3	4	12	20	
pa6	6	6	18	54	
pa7	12	6	18	144	

Table 5.4. All different combinations for the PCA file used in this report. pa3 is described in the text.

After low-pass filtering, a frequency analysis was made on three different time windows. The three selected time windows were 32, 64 and 128 points. The result is referred to as wa32, wa64, and wa128. A wavelet transformation (Kumar and Foufoula-Georgiou, 1997) into 15 components was used. The wavelet transformation can better reproduce the dynamics of short time series than the Fourier technique.

The neural networks used in the study are ordinary back propagation networks of different sizes. The output of the back propagation network is a real number. This implies that a threshold must to be selected to distinguish when the net is predicting an anomaly or not. The threshold is chosen so that the success of predicting non-anomaly is equal to the ratio between anomalies and non-anomaly, i.e. the threshold is set to give a success rate of non-anomalies to about 80% or better.

The input to the neural network is a combination of magnitudes, dynamics (wa32, wa64 and wa128) and performed on different data combinations: _all, _high, and _low. A data file containing the inputs and the desired outputs (1 if anomaly occurs within a 24

hour time window, else 0). From the created file (approximately 27500 points or rows) all rows associated with anomaly warnings (1) and twice the number of rows associated with no anomalies (0), are selected randomly to train and test the network. The training of the neural network is made with 2/3 of the data set and the test with 1/3. Normalization of the data is made using commercial network software (Neural Ware).

Table 5.5 shows some of the results using different configuration of the network and inputs. The first column is a reference number of the row. Second column, top row gives information about the data combination (the definitions are described in the text above). The bottom row of the second column indicates the level to separate the anomalies into two different cases, file fiI and fiII. The "net" indicates how many inputs and outputs used for the case and "PE" is the size of the back propagation net. Last three columns show the results from different trained network, trained with _all, fiI and fiII anomalies. For all three cases are 2/3 of the data used as a training set and 1/3 as the test. The last two files (fiI and fiII) were created using "level" in the second column. Anomalies following within 24 hours after a high value of the largest principal component (i.e. high electron fluxes) is in fiI, and the rest of the anomalies in fiII. The selected non-anomaly cases are randomly selected. In this way one network is trained to predict anomalies associated with high electron fluxes and the another network to find other causes. The "level" is set so the anomalies associated with high energy fluxes are approximately 20% of the total anomalies.

The results of the different tests in Table 5.5 are presented as the success (in percentages) of predicting the anomalies (top) and the non-anomalies (bottom) in each box. Since the output of a back propagation net is real number, the threshold for each individual test is chosen so that the non-anomaly success rate is close or higher than 80%. Since only thresholds of 0.3, 0.4 , 0.5 and 0.6 were used and only one of the results is presented in the table, a comparison between different runs in the table can be difficult.

The cases presented below are only a few of the many combinations that were tested. For more details, see WP-210-TN at http://www.geo.fmi.fi/spee/docs/

Intensities

Only the electron fluxes at the time of forecast, 24 and 48 hours before the forecast are used to train the network given in row 1 (Table 5.5 data file, pa3). The network was designed for 12 inputs, 1 output, 5 neurons in the first layer and 2 neurons in the second layer. The training of the network was made with 2/3 of the data. When tested on the unseen Meteosat-3 data (1/3), the warnings (for anomaly) were predicted correctly to 41% when 88% of the non-anomalies were correctly predicted. When testing the trained network with the full time series, the result was almost the same (40% and 88%, respectively). For the anomaly warnings, 33% of the cases were unseen and for the non-anomaly cases 66%.

Using the same set-up and training the network with only anomalies associated with the high-energy fluxes (fiI), these anomalies are predicted with the accuracy 94% (both for warnings and non-anomalies). When testing the full data set this trained network

is almost as good as from the network trained with all anomalies (if the non-anomalies are predicted with 94% accuracy the anomaly warnings are predicted with 26%).

	Traning file	**All**		**fiI**		**fiII**	
	Test file	**test**	**me**	**test**	**me**	**test**	**me**
	File comb.						
1	pa3 _all	41	40	94	26	25	32
	level.96 net9+1 PE6+2	88	88	94	94	88	91
2	pa7 _all	47	50	92	32	36	42
	level.95 net18+1 PE9+3	79	79	92	88	88	80
3	pa7 _low	46		88		27	
	level.96 net18+1 PE9+3	81		87		82	
4	pa7 _high	48		89		43	
	level.93 net18+1 PE9+3	79		91		83	
5	wa64 _all	40	39	71	34	30	33
	level.96 net15+1 PE8+2	77	79	82	83	82	83
6	pa7 wa128 _all	52	38	92	32	37	39
	level.95 net33+1 PE10+6	76	87	91	89	79	80
7	pa2 wa32	53	54	93	36	39	42
	level.95 net24+1 PE8+4	76	76	91	88	76	80
8	pa6 wa64 _all	51	40	90	40	43	42
	level.95 net33+1 PE10+4	78	88	91	84	77	77

Table 5.5. Some of the results from different neural networks. Three different training files were used for each file combination. Two different test files were used, the test file with the unseen data and the full time series of Meteosat-3 with all anomalies.

The last example in row 1 is a network trained with anomalies not directly correlated with high electron fluxes (fiII). This network is not as successful, and mainly the anomalies associated with high fluxes are predicted. When comparing the output from these networks as function of time for the full time series (with all anomalies), the network trained with fiI is easiest to analyse. The output from fiII is hardest to use, the difference between the lowest and the highest output value is small. This leads to results that are very sensitive to the selection of threshold. A small change in the threshold gives a completely different result in the forecast.

Different combinations of values from Table 5.4 have been tested, one of them is row 2 in Table 5.5. Independently of the selection, the result is more or less the same.

Dynamics

The influence of the dynamics of the electron fluxes is tested separately in row 5. All three window lengths are tested (wa32, wa64 and wa128) with the same result. The forecast

success is lower than in the previous case. When compared with row 1 and 2 the best result is for the network trained with fiII.

Combination

Combinations of values from Table 5.4 and the dynamics of the electron fluxes were also made, a few of them can be seen in rows 6-8. Independently of how the combinations were made the result was not improved compared to using only intensities. When the threshold was selected to predict 80% of the non-anomalies, the warnings were predicted with a success of 40–45%. Since the anomalies are more frequent at times with high electron fluxes the actual forecast rate of anomalies is 50–55%.

Energy interval

Information from all energy bins was used. In row 2–4 three different cases using full energy range, lower or upper range are presented. The results indicate that during events with high electron flux, all energy ranges are affected. There is no difference between the three energy ranges in the tests.

Anomaly types

The success of predicting the different types of anomalies was investigated, using one or a few of the same type. It was not possible to see if any of the anomaly types was easier to predict than the others (result not shown). The difference in some of the results can be attributed to bad statistics (too few cases).

Local times

The different local time sectors were also investigated. The warnings were indicated with the local time sector an anomaly occurred in. The predicted anomalies are predominant in the morning sector (2–10 LT) and the anomalies not predicted are evenly distributed.

5.2.7. Summary

The predicted anomalies are associated with high fluxes of electrons in the energy range 43–300 keV. Tests of different energy ranges, different types of anomalies, different combinations of data inputs and comparing different local times have been made. The anomalies on Meteosat-3 were predicted with a back propagation network. If the threshold was set to predict times without anomalies with a accuracy of 80% the warnings can be given with 40–45% accuracy (this is 50–55% of the anomalies) using on-board electron measurements.

5.3. Spacecraft anomaly forecasting using non-local environment data

In this section we study the anomaly forecasting using non-local data. In addition to the Meteosat-3 data we use anomaly data from the Swedish satellite Tele-X.

5.3.1. Tele-X

Tele-X was a broadcasting satellite owned by Nordiska Satelliteaktiebolaget, NSAB. It was launched on 2 April 1989 into a geostationary orbit at 5°E. Anomalies were registered from the 2 April 1989 (launch) until the end of the mission in 1998. The satellite is a 3-axis stabilised platform with a solar array span of 19 m. The payload mass is 170 kg.

The environment conditions considered for the design of Tele-X were: ground handling tests, launcher environment, vibrations and electromagnetic radiation, space radiation, sun incidence angles and eclipses. The considered radiation elements were: electrons trapped in the van Allen belts, low energy protons, high energy protons from solar flares and cosmic rays.

The calculated radiation dose for different parts was estimated to a maximum value of $1x10^7$ rad for sensitive equipment. Externally mounted equipment could be exposed to $5x10^7$ rad.

Code	Description	Count
1	CMU1 reset	132
2	CMU2 reset	13
3	CMU1 and CMU2 both reset	8
4	Closure of LV31/41	16
5	Closure of LV32/42	3
6	Spontaneous heater boost	2
7	OBC1 stop	14
8	OBC2 stop	2
9	OBC1/ISE1 data transfer failure	1
10	OBC2/ISE2 data transfer failure	1

Table 5.6. Anomalies on Tele-X

During the period from 2 April 1989 to 26 October 1996 192 anomalies were reported (Table 5.6). Most anomalies occurred in the Command Manager Unit (CMU) causing the command counter to reset to zero (codes 1–3). Some anomalies were causing a latch valve to spontaneously close (code 4–5). Two anomalies caused a heater to spontaneously heat to higher temperatures than intended (code 6). The on-board computer (OBC) “hanged” (code 7, 8) during the satellite lifetime, and finally contact has been lost between the OBC and the Interface Safety Electronics (ISE) (code 9–10).

The days when anomalies occurred on Meteosat-3 and Tele-X are shown in Figure 5.4, for 724 anomalies on Meteosat-3 and 192 anomalies on Tele-X. From 21 June 1988 to 20 October 1996 there were 53 days with anomalies on both Meteosat-3 and Tele-X. While only considering the anomalies (on Meteosat-3) included in the training set, from 880621–961020, there were 33 days with anomalies on both Meteosat-3 and

Tele-X. There were 26 days in total when anomalies did not occur on Tele-X but did occur on Meteosat-3. Here the anomalies on Meteosat-3 refer to the 613 anomalies used in the neural network study that focused on non-local data.

In addition, there were 81 data intervals of non-anomalies on Tele-X where anomalies on Meteosat-3 occurred during the last 4 days of the 10 days non-anomaly intervals for Tele-X. This means that 81 non-anomalies on Tele-X were associated with anomalies on Meteosat-3 with the time difference not longer than 4 days. Following the same procedure, but only comparing with the anomalies included in the training set, we obtain that the number of such non-anomalies on Tele-X is 69.

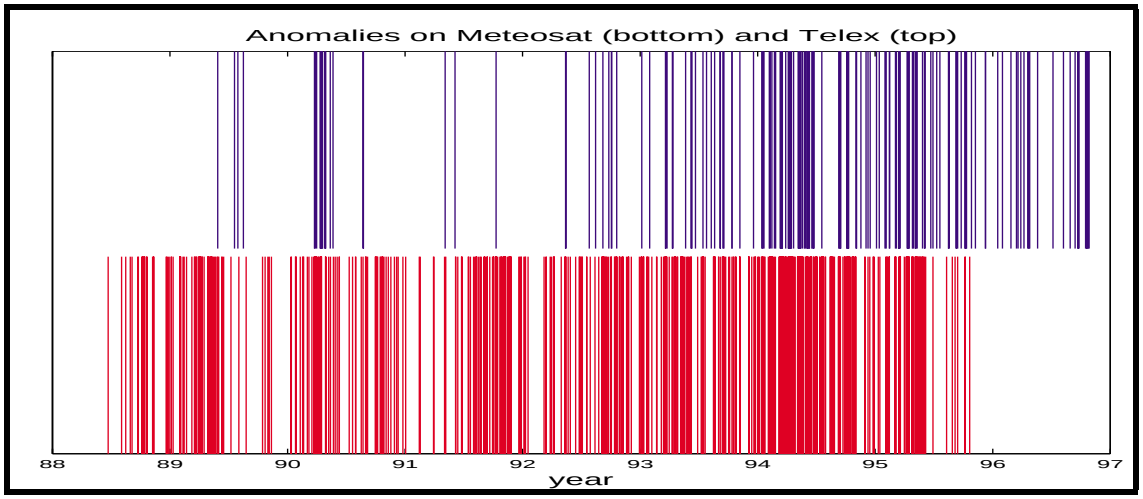

Figure 5.4. Occurrence of anomalies on Meteosat-3 and Telex-X during 880621-961020. The anomalies on Meteosat-3 are displayed on the lower panel and those on Tele-X are displayed on the upper panel.

5.3.2. Non-local environment data sets

5.3.2.1 Satellite environment data

The environment data used in this study are energetic electron flux (>2 MeV) data, from NOAA GOES space environment monitor CD-ROM. Data are from the measurements by GOES-6, GOES-7, and GOES-8. The original data are 5-minute averages. The selected data cover the period 1988–1996 because the anomaly data being investigated are from 1988–1995 on Meteosat-3 and from 1991–1996 on Tele-X. A data interval is defined to be qualified for the study if the data gaps inside the interval are less than 2 hours. After data interpolation, we averaged the data to hourly and daily resolution.

We obtain 613 data intervals qualified for the study of the 724 anomalies on Meteosat-3. Each interval is a period of 15 days and the 15th day is the day when an anomaly occurred on Meteosat-3. Likewise, we obtain 167 intervals qualified for the study of the 192 anomalies on Tele-X. Each interval also covers the period of 15 days and the 15th day is the day when an anomaly occurred on Tele-X.

A non-anomaly interval is defined as follows: if there were no anomalies on Meteosat-3 only or Tele-X only within an interval of 10 days, then the interval is selected as a non-anomaly interval. Based on this criterion, 420 (368+52) non-anomaly intervals have been found for Meteosat-3 while 140 non-anomalies are found for Tele-X, each interval with a period of 10 days and the 10th day preceding a day with no anomaly.

5.3.2.2. Geomagnetic activity data

The geomagnetic indices Kp and Dst are also used as input parameters in this study. Kp is the mean standardized K-index from 13 geomagnetic observatories between 44° and 60° northern or southern geomagnetic latitude. Dst was originally devised to describe ring current variations during the International Geophysical Year (IGY). The present Dst index is calculated from hourly H component observations at 4 low-latitude observatories. Although Kp and Dst data are continuous with no gaps, in order to use them in combination with energetic electron flux data, only the same data intervals as those of electron flux will be used for the study.

5.3.3. Forecasting anomalies using neural networks

5.3.3.1. Training, validation, and test data

Input data are the daily averaged energetic electron flux and Dst as well as the daily sum of Kp. The data of Dst, Kp and the logarithm of electron flux are normalized to the interval [–1, 1].

Training is made on 70% of the events (including anomalies and non-anomalies) on Meteosat-3 only. Neural networks are validated on the remaining 30% of Meteosat-3 events and the tested on the Tele-X data. The validation set is used to determine where the training should be terminated. The minimal validating error means that the optimal generalisation capability of neural networks has been found and that the networks can be generalised by a test set.

The training set consists of 454 anomalies and 279 non-anomalies on Meteosat-3. The validation set consists of 159 anomalies and 131 non-anomalies on Meteosat-3. The test set consists of 167 anomalies and 140 non-anomalies on Tele-X.

5.3.3.2. Time-delay neural network and learning vector quantization network

A time-delay neural network (TDNN) is a supervised learning feed-forward back-propagation network with a time delay line in the input layer. Learning Vector Quantization (LVQ) is a classification network, which assigns vectors to one of several classes. An LVQ network contains a Kohonen layer which learns and performs the classification. The input layer contains one neuron for each input parameter, the output layer contains one neuron for each class. LVQ network is a combination of supervised and un-supervised learning networks. The classes are predefined and we have a body of labelled sample

data; each sample input vector is tagged with its correct class. This is the sense of being supervised. "Un-supervision" in LVQ comes from its way of weight updating.

5.3.3.3. Forecasts using time-delay neural network

Input Kp

With Kp as input, the forecast results are summarized in Table 5.7, and are shown in Figures 5.5 (a)–(f) in terms of different time delay lines in the input layer and different number of network hidden neurons.

The quantities in Table 5.7 are specified in the following way: τ is the length of a time delay line. S is the number of hidden neurons. R_{te} is the total rate of forecast for anomalies and non-anomalies on Meteosat-3. R_{te1} is the rate of forecast for anomalies on Meteosat-3. R_{te2} is the rate of forecast for non-anomalies on Meteosat-3. R_{tlx} is the rate of forecast for anomalies and non-anomalies on Tele-X. R_{tlx1} is the rate of forecast for anomalies on Tele-X. R_{tlx2} is the rate of forecast for non-anomalies on Tele-X. R_{tr} is the training rate of forecast for anomalies and non-anomalies on Meteosat-3. R_{tr1} is the training rate of forecast for anomalies on Meteosat-3. R_{tr2} is the training rate of forecast for non-anomalies on Meteosat-3. These quantities are also applied in the following tables.

Take one of the best results for 8 days time window as an example. For anomalies on Meteosat-3, Kp can predict 78% correctly while for non-anomalies Kp can predict 80% correctly. The total forecast rate is 79%. For events on Tele-X, Kp gives the total forecast rate 64% where 78% is for anomalies and 46% for non-anomalies.

The low forecast rate for non-anomalies on Tele-X is mainly due to the definition of non-anomalies based only on one satellite. Several non-anomalies on Tele-X were selected during the data intervals where anomalies did occur on Meteosat-3. Most of these data intervals have been used to train the networks. If the networks learn most information encoded in the training set, the networks will give forecast of anomalies in response to these data intervals as the input. Therefore, the low forecast rate on non-anomalies on Tele-X is expected and is due to the definition of non-anomalies.

As the time delay line varies from 4 to 10 days and the number of network hidden neurons varies from 4 to 20, the total forecast rate varies between 71% and 79% for events on Meteosat-3 and between 62% and 68% for Tele-X. An 8-day time delay line gives slightly better accuracy than the others using Kp as the input parameter.

In summary, the forecast rate varies 71–80% for anomalies and 65–80% for non-anomalies on Meteosat-3. For Tele-X, the forecast rate varies 77–84% for anomalies and 40–51% for non-anomalies.

$\tau(days)$	S	R_{te}	R_{te1}	R_{te2}	R_{tlx}	R_{tlx1}	R_{tlx2}	R_{tr}	R_{tr1}	R_{tr2}
4	4	0.723	0.786	0.652	0.664	0.826	0.471	0.750	0.815	0.645
4	8	0.730	0.767	0.688	0.681	0.844	0.486	0.735	0.811	0.613
4	12	0.723	0.780	0.660	0.671	0.832	0.479	0.742	0.815	0.624
4	16	0.743	0.761	0.723	0.681	0.820	0.514	0.731	0.795	0.627
4	20	0.740	0.799	0.674	0.658	0.826	0.457	0.744	0.826	0.609
6	4	0.710	0.748	0.667	0.638	0.814	0.429	0.756	0.815	0.659
6	8	0.713	0.761	0.660	0.645	0.844	0.407	0.759	0.828	0.645
6	12	0.733	0.748	0.716	0.664	0.808	0.493	0.759	0.795	0.699
6	16	0.720	0.774	0.660	0.638	0.814	0.429	0.748	0.819	0.631
6	20	0.700	0.742	0.652	0.632	0.826	0.400	0.763	0.837	0.642
8	4	0.750	0.774	0.723	0.648	0.784	0.486	0.754	0.811	0.663
8	8	0.790	0.780	0.801	0.635	0.784	0.457	0.753	0.813	0.656
8	12	0.763	0.767	0.759	0.638	0.778	0.471	0.769	0.822	0.685
8	16	0.773	0.792	0.752	0.642	0.796	0.457	0.765	0.833	0.656
8	20	0.757	0.774	0.738	0.622	0.802	0.407	0.763	0.841	0.634
10	4	0.733	0.686	0.787	0.606	0.743	0.443	0.783	0.852	0.670
10	8	0.743	0.711	0.780	0.638	0.772	0.479	0.768	0.830	0.667
10	12	0.750	0.717	0.787	0.625	0.772	0.450	0.769	0.837	0.659
10	16	0.747	0.736	0.759	0.635	0.814	0.421	0.767	0.852	0.627
10	20	0.767	0.748	0.787	0.619	0.766	0.443	0.771	0.833	0.670

Table 5.7. One day ahead forecast of spacecraft anomalies from Kp (TDNN)

(a)

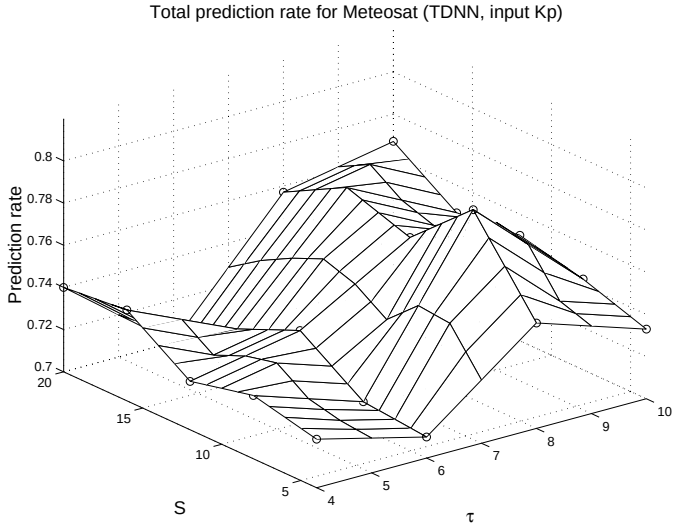
Total prediction rate for Meteosat (TDNN, input Kp)
Prediction rate
0.8
0.78
0.76
0.74
0.72
0.7
20
15
10
5
S
4
5
6
7
8
9
10
τ

(b)

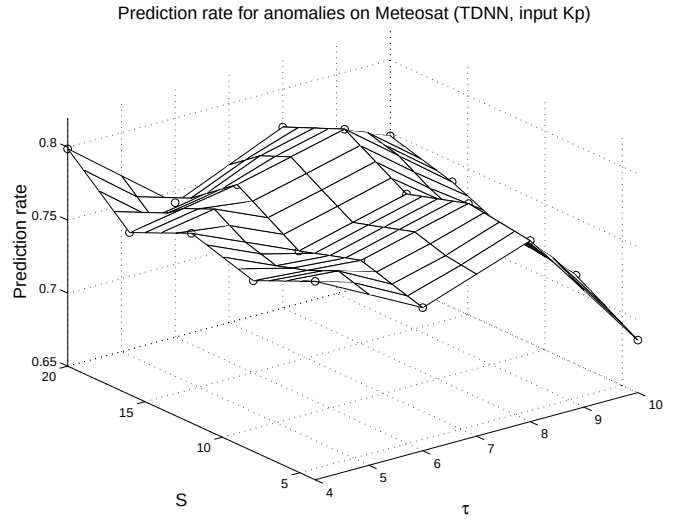
Prediction rate for anomalies on Meteosat (TDNN, input Kp)
Prediction rate
0.8
0.75
0.7
0.65
20
15
10
5
S
4
5
6
7
8
9
10
τ

(c)

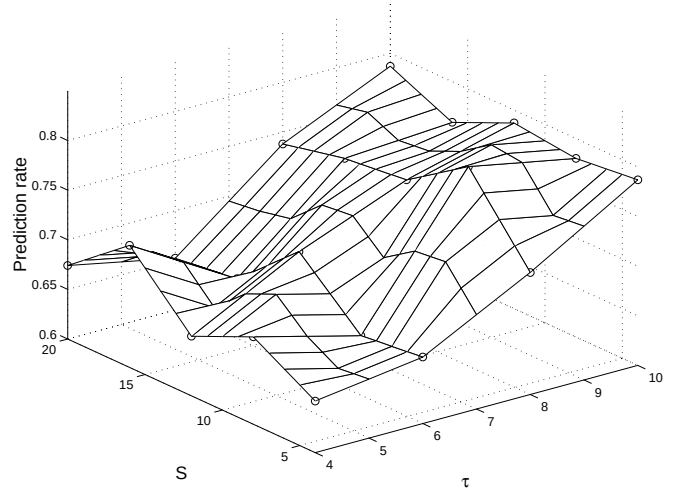
Prediction rate for non-anomalies on Meteosat (TDNN, input Kp)
Prediction rate
0.8
0.75
0.7
0.65
0.6
20
15
10
5
S
4
5
6
7
8
9
10
τ

(d)

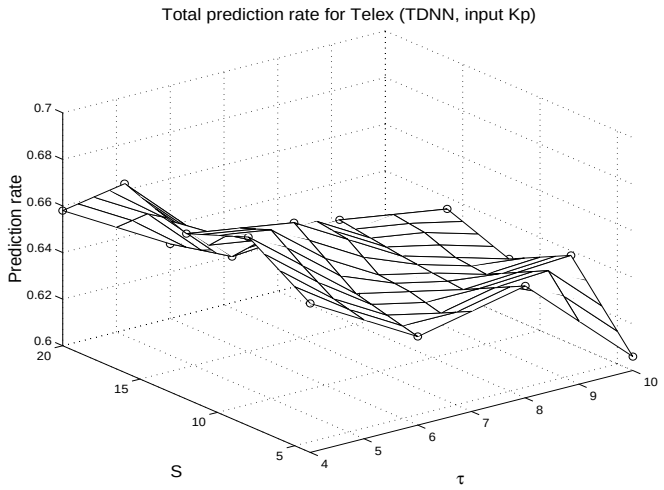

(e)

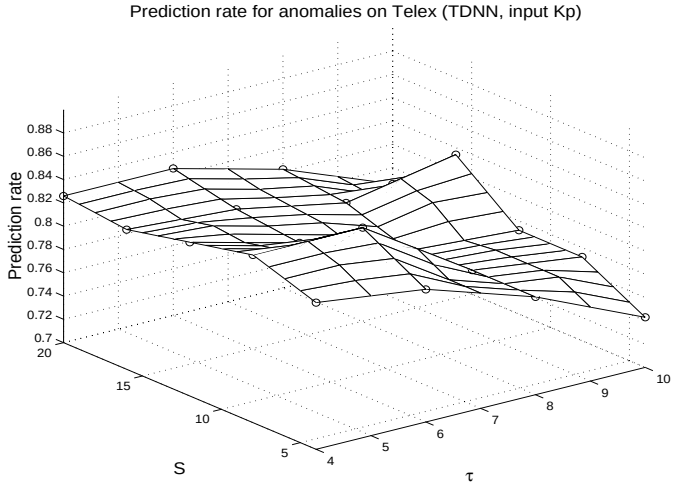

(f)

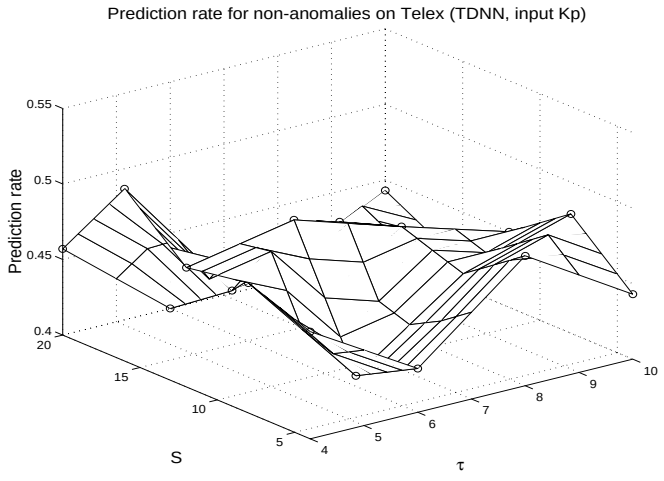

Figure 5.5. Accuracy of 1 day ahead forecast from the input Kp using TDNN in terms of the network architecture (i.e., the time delay line and the number of hidden neurons). (a-c) Total forecast rate, forecast rate for anomalies,and non-anomalies on Meteosat-3, respectively; (d-f) The same for Tele-X

Input Dst

The forecast results are given in Table 5.8 and Figures 5.6 (a)-(f) using Dst as the input parameter. When the delay line length is 8 days, the total forecast rate is 73% for events on Meteosat-3, the forecast rate is 77% for anomalies and 67% for non-anomalies on Meteosat-3. The total forecast rate is 65% for events on Tele-X, the forecast rate is 81% for anomalies and 44% for non-anomalies on Tele-X. A 10- or 8-day delay line results in similar forecast accuracy.

The total forecast accuracy is rather stable in terms of time delay line and number of hidden neurons with Dst as input. The total forecast rate varies 69–73% for events on Meteosat-3 while the total forecast rate varies between 62–66%.

The forecast rate varies 70–80% for anomalies and 56–72% for non-anomalies on Meteosat-3. For Tele-X, the forecast rate varies 77–84% for anomalies and 41–46% for non-anomalies.

Input electron flux (E > 2 Mev)

For the electron flux as the input parameter we summarize the forecast results in Table 5.9 and Figures 5.7 (a)-(f) in terms of the time delay line and the number of the network hidden neurons.

As can be seen from Table 5.9, the total forecast rate varies between 52% and 62% for the events (included in the validation set) on Meteosat-3, the forecast rate is in the range 57–86 % for anomalies on Meteosat-3 and in the range 33–53 % for non-anomalies on Meteosat-3. For Tele-X, the total forecast rate ranges from 61% to 67%, the forecast rate ranges from 74% to 93% for anomalies and from 32% to 49% for non-anomalies.

The energetic electron flux tends to predict anomalies much more accuartely than to predict non-anomalies. It might well imply that if energetic electron flux is high, then anomalies will probably occur and that if energetic electron flux is low, it is still possible to have an anomalies which is caused by some other factors, e.g. low energy electron flux. When we look at training error, it can be found that training accuracy (above 80%) for anomalies is much higher than that (37% to 62%) for non-anomalies. We can see from the training that the energetic electron flux is not able to well predict non-anomalies.

In contrast, when the input is Kp and Dst, respectively, during training the training accuracy ranges between 61% and 70% for the input Kp and ranges between 64% and 72% for the input Dst.

$\tau(days)$	S	R_{te}	R_{te1}	R_{te2}	R_{tlx}	R_{tlx1}	R_{tlx2}	R_{tr}	R_{tr1}	R_{tr2}
4	4	0.687	0.799	0.560	0.651	0.844	0.421	0.759	0.826	0.649
4	8	0.693	0.792	0.582	0.651	0.844	0.421	0.757	0.826	0.645
4	12	0.700	0.774	0.617	0.661	0.832	0.457	0.749	0.804	0.659
4	16	0.693	0.792	0.582	0.661	0.844	0.443	0.754	0.819	0.649
4	20	0.690	0.786	0.582	0.651	0.844	0.421	0.761	0.828	0.652
6	4	0.707	0.748	0.660	0.635	0.814	0.421	0.769	0.833	0.667
6	8	0.707	0.748	0.660	0.622	0.802	0.407	0.761	0.830	0.649
6	12	0.707	0.748	0.660	0.625	0.802	0.414	0.764	0.833	0.652
6	16	0.713	0.704	0.723	0.625	0.772	0.450	0.760	0.782	0.724
6	20	0.700	0.730	0.667	0.622	0.790	0.421	0.756	0.815	0.659
8	4	0.720	0.786	0.645	0.651	0.826	0.443	0.772	0.835	0.670
8	8	0.710	0.723	0.695	0.635	0.796	0.443	0.759	0.811	0.674
8	12	0.723	0.780	0.660	0.648	0.832	0.429	0.765	0.828	0.663
8	16	0.727	0.774	0.674	0.645	0.814	0.443	0.768	0.824	0.677
8	20	0.713	0.748	0.674	0.642	0.820	0.429	0.763	0.826	0.659
10	4	0.733	0.748	0.716	0.642	0.808	0.443	0.772	0.828	0.681
10	8	0.730	0.774	0.681	0.658	0.832	0.450	0.778	0.844	0.670
10	12	0.727	0.742	0.709	0.645	0.820	0.436	0.779	0.839	0.681
10	16	0.730	0.761	0.695	0.648	0.826	0.436	0.775	0.844	0.663
10	20	0.720	0.767	0.667	0.655	0.832	0.443	0.778	0.844	0.670

Table 5.8. One day ahead forecast of spacecraft anomalies from Dst (TDNN)

(a)

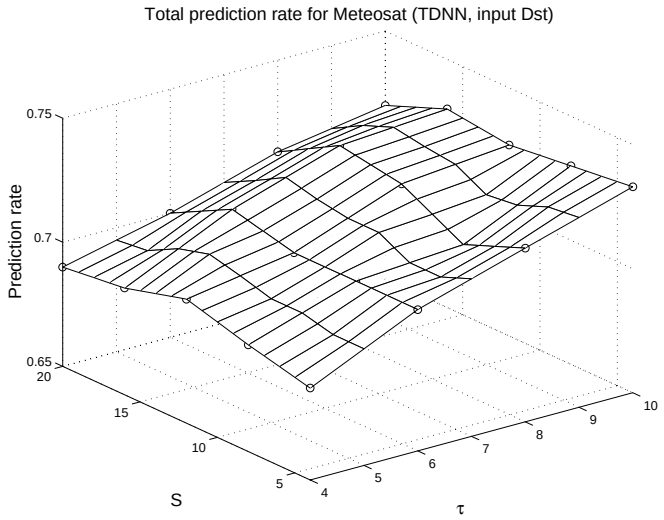
Total prediction rate for Meteosat (TDNN, input Dst)
Prediction rate
0.75
0.7
0.65
20
15
10
5
S
4
5
6
7
8
9
10
τ

(b)

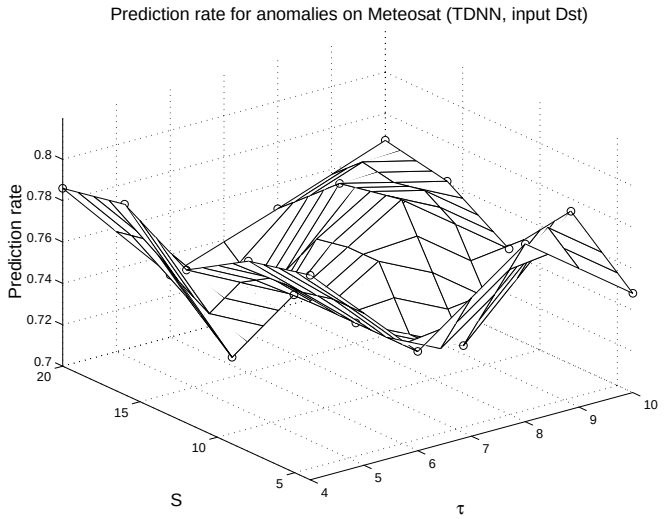
Prediction rate for anomalies on Meteosat (TDNN, input Dst)
Prediction rate
0.8
0.78
0.76
0.74
0.72
0.7
20
15
10
5
S
4
5
6
7
8
9
10
τ

(c)

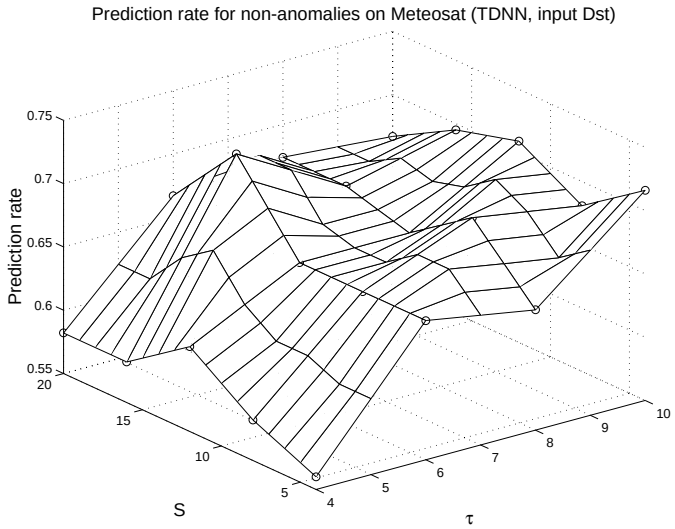
Prediction rate for non-anomalies on Meteosat (TDNN, input Dst)
Prediction rate
0.75
0.7
0.65
0.6
0.55
20
15
10
5
S
4
5
6
7
8
9
10
τ

(d)

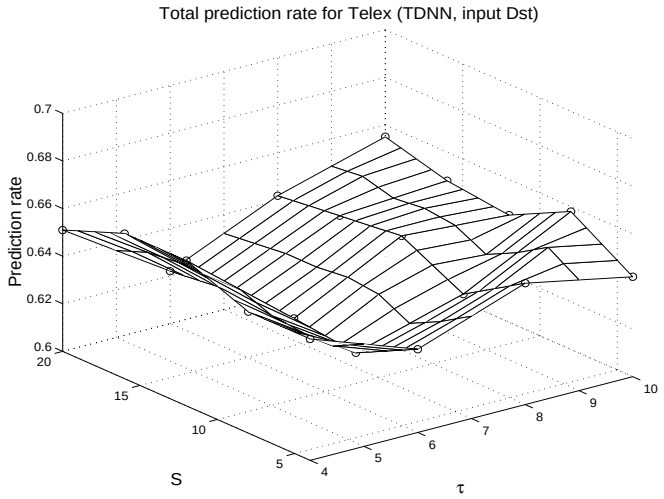

(e)

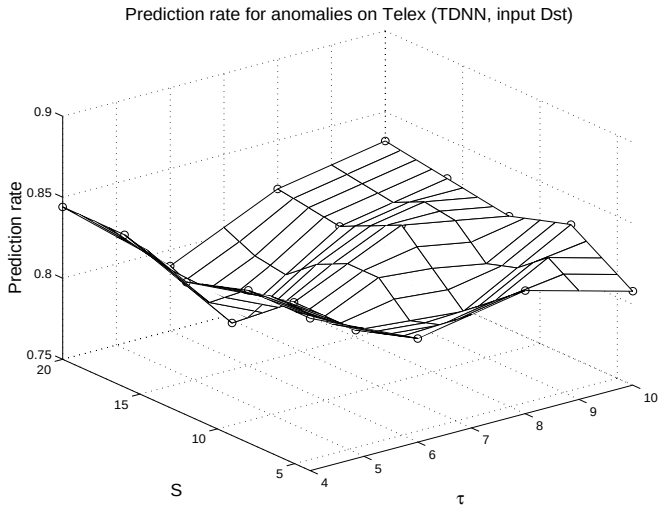

(f)

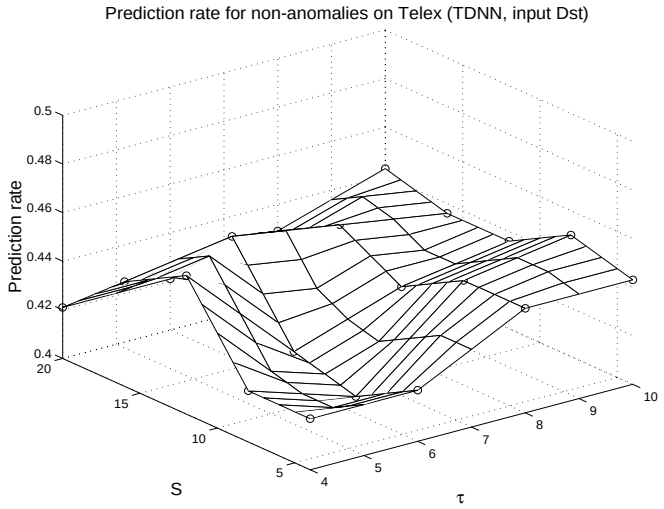

Figure 5.6. Same as Figure 5.5 but using Dst as input.

$\tau(days)$	S	R_{te}	R_{te1}	R_{te2}	R_{tlx}	R_{tlx1}	R_{tlx2}	R_{tr}	R_{tr1}	R_{tr2}
4	4	0.587	0.761	0.390	0.648	0.868	0.386	0.675	0.813	0.452
4	8	0.620	0.862	0.348	0.674	0.934	0.364	0.673	0.861	0.366
4	12	0.613	0.836	0.362	0.648	0.886	0.364	0.681	0.850	0.405
4	16	0.593	0.811	0.348	0.648	0.892	0.357	0.674	0.848	0.391
4	20	0.593	0.704	0.468	0.642	0.772	0.486	0.643	0.696	0.556
6	4	0.577	0.736	0.397	0.642	0.868	0.371	0.692	0.830	0.466
6	8	0.587	0.761	0.390	0.622	0.862	0.336	0.679	0.824	0.444
6	12	0.580	0.792	0.340	0.625	0.880	0.321	0.670	0.835	0.401
6	16	0.540	0.623	0.447	0.642	0.826	0.421	0.675	0.760	0.538
6	20	0.540	0.723	0.333	0.651	0.880	0.379	0.682	0.835	0.434
8	4	0.583	0.780	0.362	0.651	0.862	0.400	0.690	0.848	0.434
8	8	0.547	0.635	0.447	0.635	0.796	0.443	0.696	0.778	0.563
8	12	0.573	0.723	0.404	0.629	0.832	0.386	0.696	0.837	0.466
8	16	0.563	0.673	0.440	0.635	0.826	0.407	0.707	0.835	0.498
8	20	0.573	0.717	0.411	0.619	0.826	0.371	0.709	0.846	0.487
10	4	0.560	0.667	0.440	0.651	0.820	0.450	0.704	0.815	0.523
10	8	0.563	0.679	0.433	0.629	0.832	0.386	0.697	0.846	0.455
10	12	0.553	0.610	0.489	0.629	0.820	0.400	0.737	0.833	0.581
10	16	0.520	0.629	0.397	0.609	0.802	0.379	0.722	0.837	0.534
10	20	0.550	0.572	0.525	0.609	0.743	0.450	0.744	0.822	0.616

Table 5.9. One day ahead forecast of spacecraft anomalies from electron flux (TDNN)

(a)

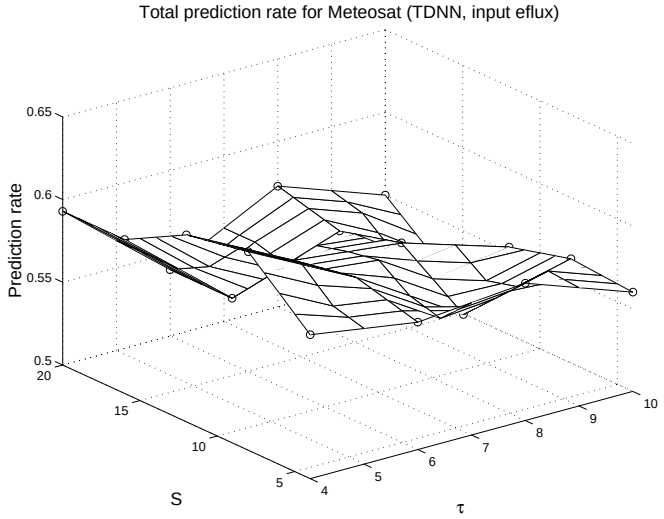
Total prediction rate for Meteosat (TDNN, input eflux)
Prediction rate
0.65
0.6
0.55
0.5
20
15
10
5
S
4
5
6
7
8
9
10
τ

(b)

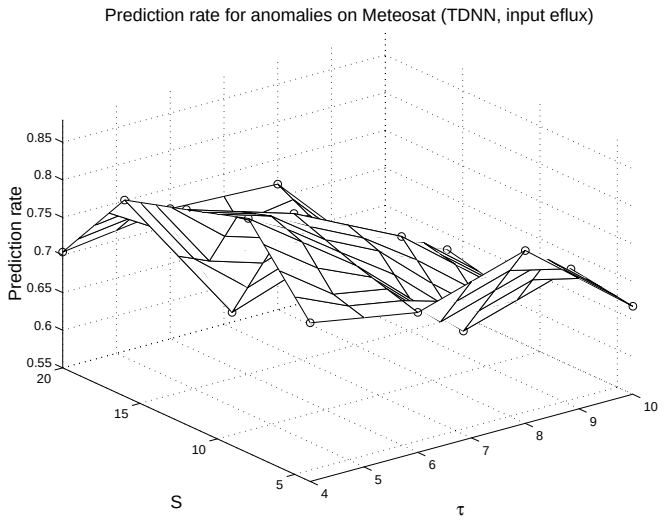
Prediction rate for anomalies on Meteosat (TDNN, input eflux)
Prediction rate
0.85
0.8
0.75
0.7
0.65
0.6
0.55
20
15
10
5
S
4
5
6
7
8
9
10
τ

(c)

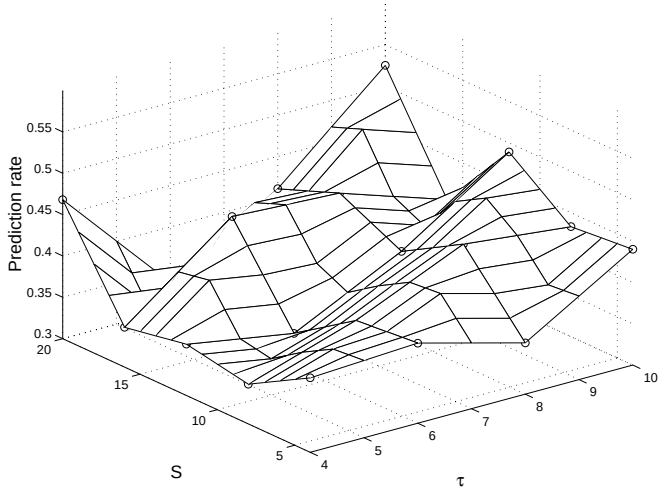
Prediction rate for non-anomalies on Meteosat (TDNN, input eflux)
Prediction rate
0.55
0.5
0.45
0.4
0.35
0.3
20
15
10
5
S
4
5
6
7
8
9
10
τ

(d)

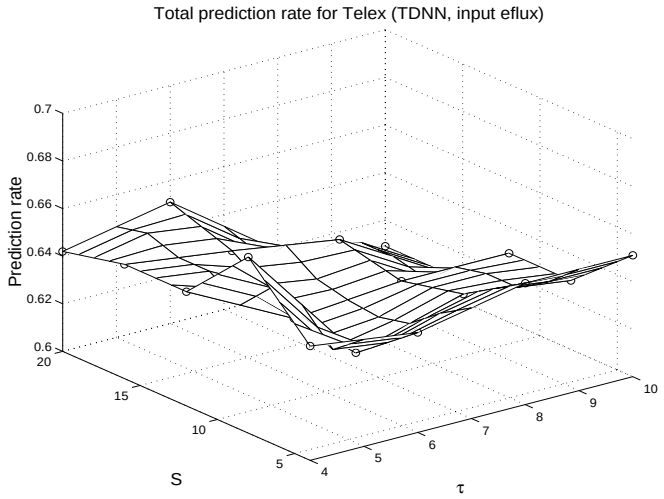

(e)

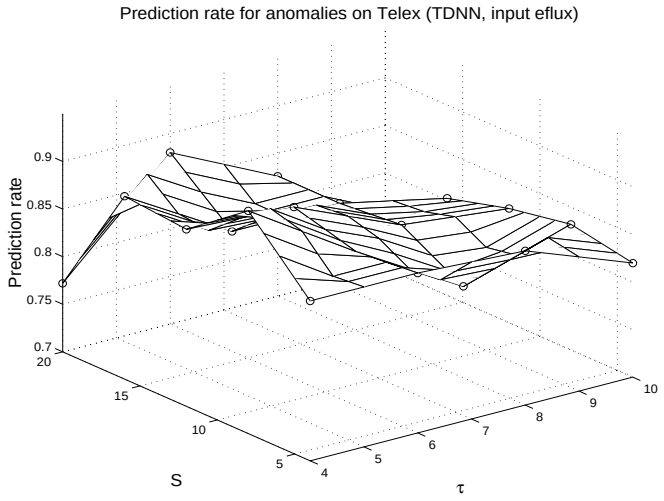

(f)

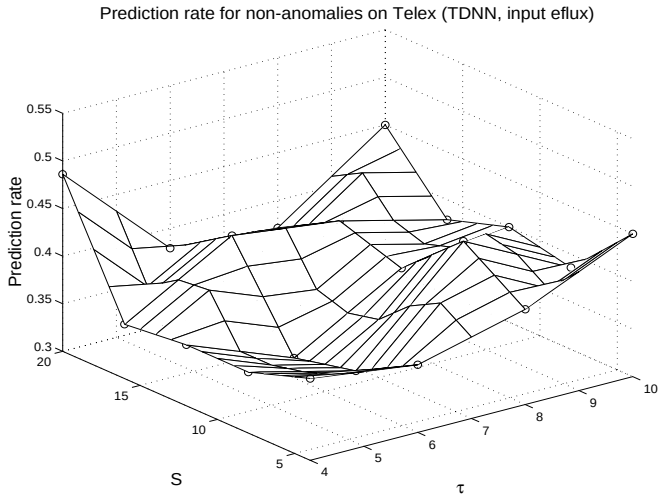

Figure 5.7. Same as Figure 5.5 but using energetic electron flux (E > 2 Mev) as input.

5.3.3.4. Forecasts using learning vector quantization network

We have used two network classes (TDNN and LVQN) and found that they give similar forecast accuracy. Therefore, we mainly focus on TDNN. In order for a comparison, we present the results as the input is Kp and energetic electron flux.

Input Kp

The forecast results are given in Table 5.10. Comparing Table 5.8 and Table 5.10 we see that the two network classes give similar accuracy.

$\tau(days)$	S	R_{te}	R_{te1}	R_{te2}	R_{tlx}	R_{tlx1}	R_{tlx2}	R_{tr}	R_{tr1}	R_{tr2}
4	6	0.730	0.805	0.645	0.671	0.814	0.500	0.722	0.782	0.624
4	10	0.717	0.723	0.709	0.658	0.707	0.600	0.697	0.716	0.667
4	14	0.733	0.742	0.723	0.664	0.766	0.543	0.726	0.749	0.688
4	18	0.740	0.736	0.745	0.687	0.772	0.586	0.727	0.736	0.713
6	6	0.710	0.723	0.695	0.655	0.778	0.507	0.689	0.729	0.624
6	10	0.727	0.723	0.730	0.648	0.725	0.557	0.724	0.742	0.695
6	14	0.743	0.736	0.752	0.674	0.784	0.543	0.718	0.744	0.674
6	18	0.740	0.730	0.752	0.661	0.784	0.514	0.738	0.771	0.685
8	6	0.767	0.755	0.780	0.638	0.796	0.450	0.746	0.793	0.670
8	10	0.790	0.761	0.823	0.635	0.778	0.464	0.739	0.791	0.656
8	14	0.807	0.792	0.823	0.645	0.820	0.436	0.759	0.813	0.670
8	18	0.797	0.748	0.851	0.671	0.772	0.550	0.741	0.775	0.685
10	6	0.777	0.736	0.823	0.612	0.766	0.429	0.718	0.780	0.616
10	10	0.763	0.667	0.872	0.645	0.743	0.529	0.741	0.769	0.695
10	14	0.777	0.698	0.865	0.642	0.731	0.536	0.737	0.758	0.703
10	18	0.813	0.742	0.894	0.655	0.737	0.557	0.763	0.797	0.706

Table 5.10. One day ahead forecast of spacecraft anomalies from Kp (LVQNN)

Input electron flux (E > 2 Mev)

With electron flux as the input, the results are given in Table 5.11. The accuracy is slightly lower than that using TDNN.

5.3.4. Discussion

With Kp as the input parameter, the accuracy is as high as 80% at the best. With Dst as the input parameter, the accuracy is slightly lower than that in the case of Kp as input. This 3-hour planetary index Kp was introduced by Bartels (1949) and is designed to measure solar particle radiation by its magnetic effects. Kp is derived from the standardized K-index from 13 geomagnetic observatories between 44 degrees and 60 degrees

northern or southern geomagnetic latitude. Dst was originally devised by Sugiura (1964) to describe ring current variations during the International Geophysical Year (IGY). The present Dst index is calculated hourly from the H component recorded at 4 low-latitude magnetic observatories. All of these observatories are about equally spaced in longitude (i.e. evenly distributed in local time) and at low latitudes, 20°-30° away from the dipole equator where both auroral- and equatorial-electrojet effects are minimal. Therefore, Kp is a more global indicator of geomagnetic activity than Dst. The forecast accuracy obtained with Kp or Dst as the input parameter is reasonable in comparison. The reason that Kp is the best candidate for predicting anomalies and non-anomalies of satellites is not only the accuracy but also its availability in real-time. The estimated Kp is available in real-time (http://www.sel.noaa.gov/planetary_k.html).

$\tau(days)$	S	R_{te}	R_{te1}	R_{te2}	R_{tlx}	R_{tlx1}	R_{tlx2}	R_{tr}	R_{tr1}	R_{tr2}
6	6	0.543	0.654	0.418	0.645	0.760	0.507	0.614	0.696	0.480
6	10	0.513	0.604	0.411	0.704	0.778	0.614	0.628	0.685	0.534
6	14	0.557	0.629	0.475	0.678	0.772	0.564	0.628	0.705	0.502
6	18	0.527	0.572	0.475	0.671	0.760	0.564	0.656	0.731	0.534
8	6	0.583	0.792	0.348	0.648	0.832	0.429	0.622	0.747	0.419
8	10	0.537	0.597	0.468	0.687	0.754	0.607	0.608	0.630	0.573
8	14	0.527	0.623	0.418	0.674	0.784	0.543	0.632	0.707	0.509
8	18	0.550	0.572	0.525	0.681	0.760	0.586	0.640	0.676	0.581

Table 5.11. One day ahead forecast of spacecraft anomalies from eflux (LVQNN)

Dst is not available in real-time. But we can accurately predict Dst 1-2 hours ahead with the real-time solar wind input from WIND or ACE satellite (Wu, 1997; Wu et al., 1998). Hence we can have real-time forecast of Dst which can be used for the study of satellite anomalies.

With the energetic electron flux as the input, the forecast accuracy is relatively lower, mainly due to the lower accuracy of non-anomalies. We argue that the reasons are twofold. One is the energetic electron flux (E > 2 Mev) is not the only factor causing anomalies on satellites, for example if the anomalies is caused by surface charging. The lower energy electron flux could be an important factor causing anomalies due to, e.g., surface charging. In other words, if energetic electron flux was high, there would be anomalies occurring on satellites. However, if energetic electron flux was low, the possibility for an anomaly to occur still exists (due to low energy electron flux).

To completely describe how satellite anomalies are caused by electron flux, we will need electron flux data with energy from low (the order of keV) to high (the order of MeV). This will be able to give a better forecast accuracy.

The definition of non-anomalies is based only on one satellite. If we train the neural networks on one satellite and test on the same satellite, the accuracy will not be affected much since the distribution of local conditions on the satellite in the training set and in the test set will not be much different. But if we train on events on one satellite and test on events on the other. The error will originate from the different local conditions and local environments on different satellites. Since this study is focused on using nonlocal space environment data, it has been presumed that the local conditions and local environments are the same on different satellites, although this is not a good approximation in reality.

To reduce the error caused by different local conditions and local environments, we have to have a definition of non-anomalies as strict as possible by taking into account as many satellites as possible. It means that the definition of non-anomalies is satellite-independent. This will give a better forecast accuracy for non-anomalies and for anomalies as well. However, another problem will be raised. That is, we do not know how accurately our neural network models can generalise from one satellite to another. Therefore, while combining nonlocal data with local data as input, this problem might be solved to a large extent.

The training was on Meteosat with the threshold of 0.5. For the results given in Tables 5.7-5.9, the threshold for an output (of TDNN) to be an anomaly or a non-anomaly is 0.5. The specific criterion is that, if the value of the TDNN output is in the range (0.5 1.5), then the output gives an anomaly forecast and if the value of the TDNN output is in the range (-0.5 0.5) then the output gives a non-anomaly forecast. The local conditions of Tele-X are different from Meteosat. We can expect when how neural network models will not generalise well from one satellite to another since the definition of non-anomalies is satellite-dependent. To have a better generalisation from one satellite (Meteosat) to another (Tele-X), we try to find a new threshold value for a network output to determine if the output is an anomaly or a non-anomaly for Tele-X. We investigate whether or not the threshold value is satellite-dependent. In other words, we examine if such a threshold value exists that forecast accuracy for anomalies and for non-anomalies is very close to each other as the case for Meteosat with the threshold of 0.5. Nonetheless, it should be noted that the total forecast rate will be unchanged.

For forecasts on Tele-X, as we can see from Tables 5.7–5.9, the forecast accuracy for non-anomalies is much lower than for anomalies. Therefore we vary the value of threshold for 2 neural network models (for input Kp and 8-day time window) respectively with 8 and 16 hidden neurons. We obtain the forecast results for Tele-X in Table 5.12 and Figure 5.8. As seen from Figure 5.8, we have found a new threshold value which can give better accuracy of non-anomalies at the expense of accuracy for anomalies. This threshold value is 0.63, giving forecast rate of about 65 percent for both anomalies and non-anomalies. The two different models give almost the same value of threshold. Anomaly or non-anomaly forecast accuracy varies with the threshold value in

the same way for the two network models. In order to confirm the threshold of 0.63 is valid in all cases, we need to do some more investigations. However, at least it indicates that the difference of local conditions of different satellites might be described by the value of the threshold.

$\tau(days)$	S	Threshold	R_{tlx}	R_{tlx1}	R_{tlx2}
8	8	0.40	0.635	0.898	0.300
8	8	0.50	0.635	0.784	0.457
8	8	0.55	0.635	0.743	0.529
8	8	0.60	0.635	0.701	0.586
8	8	0.65	0.635	0.653	0.707
8	8	0.70	0.635	0.599	0.771
8	16	0.40	0.642	0.880	0.307
8	16	0.50	0.642	0.796	0.457
8	16	0.55	0.642	0.760	0.529
8	16	0.60	0.642	0.701	0.600
8	16	0.65	0.642	0.635	0.700
8	16	0.70	0.642	0.581	0.764

Table 5.12. One day ahead forecast accuracy on Tele-X from Kp (TDNN) vs threshold value.

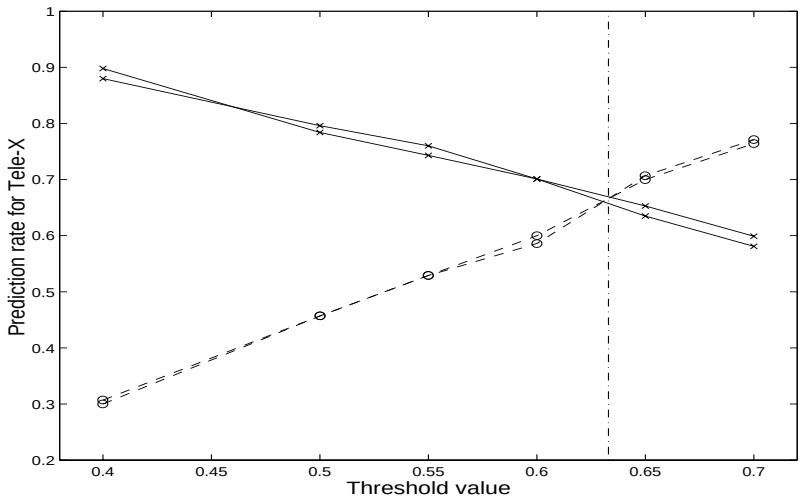

Figure 5.8. The forecast accuracy for Tele-X versus the threshold value. The solid line represents the forecast for anomalies on Tele-X and the dashed line represents the forecast for non-anomalies on Tele-X.

5.4.Spacecraft anomaly forecasting using heterogeneous environment data

In the previous sections anomaly forecasting using local and non-local data were analyzed separately. In both studies the environmental data were used to predict anomalies on GEO spacecraft.

5.4.1. Heterogeneous data

The data files for predicting spacecraft anomalies in Section 5.2.6. were expanded to be used with a heterogeneous data set. The Kp- and Dst-indices were included with 2-hour resolution (the Kp index is normally given as a three-hour index) to comply with the rest of the data set. The anomalies from both the Tele-X satellite and Meteosat-3 were used.

5.4.2 Test of different combinations

Table 5.13 shows the result of some of the trained networks. The first column shows the number of the row, the second how the data set is combined and the last four columns indicate on which data set the back propagation net has been trained; Meteosat-3, Tele-X, the fiI (described in Section 5.2.6.) and fiII. For each trained net 2/3 of the anomalies are used to train the net and 1/3 to test the net. The result for each tested net is shown in the column marked test. Since the non-anomalies are much more common, each net is tested with the full time sequence of Meteosat-3 (me) and Tele-X data (te). Note the order between me and te is reversed for the network trained with Tele-X anomalies in the Table. The results for the different tests are presented as the success (in percentages) of predicting the anomalies (top) and the non-anomalies (bottom) in each box. Since the output of a back propagation net is a real number the threshold for each individual test is chosen so that the non-anomaly success rate is close to or higher than 80%. Only the thresholds of 0.3, 0.4 , 0.5 and 0.6 were used.

<u>Electron fluxes</u>

In rows 1 and 2 the data are selected in a similar way as in Section 5.2.6. The result for the network trained with all Meteosat-3 anomalies, only the anomalies associated with high fluxes (fiI) and the anomalies not in fiI (fiII) is the same as in Section 5.2.6. The network is also trained to predict Tele-X anomalies. The success rate for the Tele-X anomalies is higher than for Meteosat-3. If the non-anomalies are to be 87% correctly predicted, the Tele-X anomalies are predicted to 60%.

When the full time series of Meteosat-3 is used as a test file on the network trained with Tele-X anomalies, the result is almost equally good as if the full time series of Meteosat-3 is tested on a network trained with Meteosat-3 (row 1 high lighted). This was also true the other way around using the full time series of Tele-X (not shown).

	Training file	**Meteosat**		**Tele-X**			**fiI Meteosat-3**			**fiII Meteosat-3**		
	Test file	**test**	**me**	**test**	**te**	**me**	**test**	**me**	**te**	**test**	**me**	**te**
	File comb.											
1	pa3 _all	41	**40**	60	54	**39**	94	26	38	50	59	72
	level.96 net12+1 PE6+2	88	**88**	87	86	**89**	94	94	92	72	73	70
2	wa64 _all	40	39	44	43	37	71	34	37	30	33	33
	level.96 net15+1 PE8+2	77	79	77	77	79	82	83	81	82	83	80
3	Kp 10x12 (_all)	43	42	50	49	49	85	23	30	31	33	34
	level.96 net10+1 PE5+2	89	88	89	88	82	94	96	94	87	88	85
4	Dst 10x12 (_all)	53	35	62	61	48	88	24	30	14	15	16
	level.96 net10+1 PE5+2	77	89	78	78	81	94	95	92	94	94	93
5	pa3 dst 3x24 _all	54	41	68	51	34	96	22	31	38	41	48
	level.96 net12+1 PE6+2	80	89	82	89	91	95	96	94	82	84	80
6	pa3 kp 3x24 _all	55	53	67	53	36	92	24	34	47	49	55
	level.96 net12+1 PE6+2	81	81	79	88	91	96	96	94	75	76	73
7	pa3 wa64 kp+dst 10x12 _all	**47**	49	**64**	67	40	92	21	28	38	40	44
	level.96 net44+1 PE20+10	**87**	87	**86**	85	87	98	96	94	85	86	82
8	pa3 month(1/2 year) _all	47	47	60	71	52	88	41	59	37	36	38
	level.95 net10+1 PE5+2	80	79	88	76	80	94	82	83	79	81	80
9	pa3 year _all	47	41	63	75	51	86	42	55	45	49	45
	level.95 net10+1 PE5+2	80	81	87	78	82	93	84	85	76	79	87
10	pa3 hour _all	50	51	54	66	46	95	42	61	32	33	40
	level.95 net10+1 PE5+2	79	81	89	78	80	85	82	82	82	85	83
11	pa3 4x18Kp+Dst hh mm yy	57	51	69	79	37	**96**	**46**	**63**	54	50	41
	level.95 net20+1 PE5+2	78	83	85	78	88	**88**	**81**	**80**	74	74	82
12	pa3 4x18Kp+Dst hh mm yy	57	50	70	82	41	97	46	63	55		51
	level.95 net20+1 PE10+4	78	84	85	79	87	88	81	80	74		82
13	1 output=Meteosat+Tele-X	62	63				76	58		38	62	
	All the rest as test 11	79	80				85	81		87	79	
14	as test 11 + time since last	52	53				95	43		48	43	
	meteosat anomaly	81	80				89	83		77	78	
	level.95 net18+1 PE5+2											

Table 5.13. Forecast result of anomalies on Meteosat-3 and the Tele-X satellites. Different data sets and back propagation nets have been used. The numbers show the success rate in percentages for anomalies (top value in each box) and non anomalies (lower value in each box). See text for further details.

Kp index

In Section 5.3. the Kp-index was used to predict anomalies on the satellite. In this test we created the data set slightly differently in order to combine the Kp index to the dataset created in Section 5.2.6. In row 3 ten values of the Kp-index have been used as input to the

neural network. The 10 values were a combination of data at the time of forecast and then 9 previous Kp values spread out with 12 hour time steps between each other. In row 3 this is indicated as Kp 10x12. Comparing row 3 with row 1 the success for the different tests is equal, the electron fluxes from the Meteosat-3 satellite is as good as the Kp-index. This is not surprising since the Kp-index shows the level of geomagnetic activity (Wrenn and Sims, 1993).

Forecasts using electron fluxes from Meteosat-3 (row 1) had a higher success rate for Tele-X than for Meteosat-3. In the case using Kp to predict anomalies the success rate between the two satellites is more equal.

Dst index

In the same way as for Kp, the Dst was tested (row 4). In this test, as in Section 5.3, Dst is not as good to predict anomalies as Kp.

Combination

In rows 5 - 7 the electron fluxes measured on the Meteosat-3 are combined with the Kp- and Dst-indices with different resolution. Different combinations of local and non-local data are made. The improvement between row 1-4 and row 7 (high lighted) is approximately 5 %.

Time of year

The frequency of anomaly occurrence as function of; time of year, time in solar cycle, and the local time were studied for both Meteosat-3 and Tele-X. In row 8 the year has been devided into two parts centered around equinox, giving a 6 month period. The input to the net is the electron flux from pa3 (see Table 5.4) and the month. The information of the time of the year does not improve the result. The peaks at equinox are already in the electron flux data. Explicit information of the time of year is thus not needed.

Time in solar cycle

The phase of the solar cycle was used ranging year 1988 (0) to the end of the Meteosat-3 mission (7). When the net trained (row 9) on Tele-X anomalies, it was trained only for times from year 4 and higher. When the Meteosat-3 data are tested with the full seven years of data, the first years of data will not be predicted. This indicates that unless the information of the full solar cycle exists, one shall be careful to introduce the explicit information of the phase in the solar cycle. Row 9 shows Meteosat-3 result using only the same time period as the Tele-X satellite.

Universal time

Local time is difficult to use since the two satellites are not at the same location and Meteosat-3 was moved to different positions during its lifetime. For this reason the UT time was used instead (row 10). The spacecraft are not far away from each other. Again the difference of anomaly occurrence with respect to the local time is already in the information of the electron flux.

Information on latest anomaly

Another test (row 14) was made to see if information about the last anomaly occurrence improves the forecast result. Wrenn and Sims (1993) suggested that for deep-dielectric charging the successive switching is some 30 hours. This means that the satellite needs time after a discharge to build up a new potential. The test did not give any improvement in forecast success of the Meteosat-3 anomalies. Possible explanation for the result may be that there are few anomalies that are close in time to each other, giving rise to bad statistics when using all anomalies.

Combine all

In row 11 and 12 a larger combination of inputs is used. The improvement is not significant. Figure 5.9 shows the results of the four different nets from row 11. The time period in the figure is the time when both satellites were operational. Four curves in four different panels are shown; from bottom Meteosat-3, Tele-X, fiI and fiII data used to train the net. At the top the desired output for Meteosat-3 (lower) and the Tele-X (higher) are indicated by squared lines.

Combination of Meteosat-3 and Tele-X

In row 13 the input to the network is the same as in row 11 but the desired output is a combination of Meteosat-3 and Tele-X, one (1) if one of the two satellites has an anomaly within 24 hour otherwise zero (0). The result is not much different from the previously trained networks. The difference is mainly due to the fact that more anomalies exist in the data set. The anomalies that were previously not predicted are still not predicted.

5.4.3 Summary

The anomaly warnings on Meteosat-3 and Tele-X are predicted using different inputs. When the non-anomalies are predicted with approximately 80% accuracy, the success rates for anomalies are 60% and 70% respectevly. This is better than only using the local electron data or one of the indices, Kp or Dst.

Using these data for forecast the clearest output signal is given when the neural net is trained with only warnings associated with high fluxes. If one allows the success to predict the non-anomalies to 80% the warnings can be predicted to 47% (this is about 57% of the total anomalies) for the net trained on the high fluxes. The net trained with the anomalies associated to high fluxes gives the output that is easiest to use for an operator. The net trained on anomalies not associated with high fluxes is better to predict the start of a period of high fluxes.

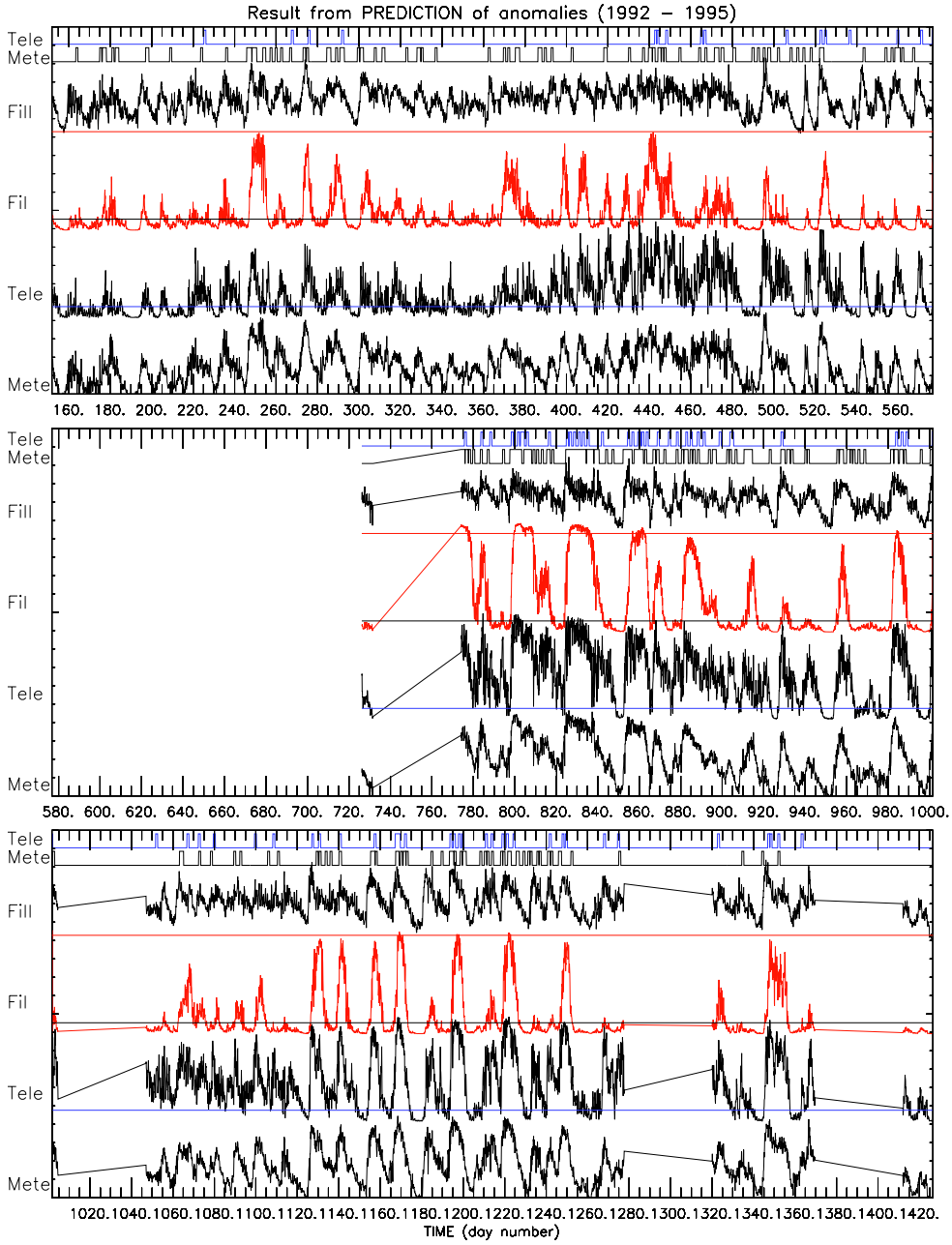

Figure 5.9 The result from the different networks (row 11). The time series covers 1992 to 1995. There were time gaps when the SEM-2 was not operated. From bottom is the output result from the net trained with; Meteosat-3 , Tele-X, fiI and fiII. At the top are the anomalies from Meteosat-3 and Tele-X represented as a squared line. The square lines are 12 points (one day) and the anomaly occurred at the end of the block.

5.5 Discussion of anomaly forecasting

It seems feasible to construct an automatic system producing warnings based on information on energetic electron fluxes, possibly combined with near-real-time information on geomagnetic or solar activity. A warning can be given about 24 hours ahead of the time for increased risk of anomalies. Environment monitors should always be included onboard spacecraft; Not only to give possibilities to predict times with higher risk for damage of components or system failures but also to provide data together with instruments on other spacecraft that can help us to better understand the space environment. Long time series will be needed to separate long-term effects from variations on shorter time-scales. This type of investigation can be compared to the importance to have long time series of ground temperature measurements to understand the climate changes on the Earth.

The neural network could only find the anomalies that are associated with intense energetic electron fluxes. Three measurements of the fluxes preceding the forecast seems to be enough for the forecast.

Wrenn (1995) and Wrenn and Sims (1996) analyzed anomalies on the satellite DRA δ together with electron fluxes from GOES (>2 MeV) and Meteosat-3 (>0.2 MeV), from March 1991 to March 1994. The anomalies on DRA δ were similar to the Meteosat and Tele-X anomalies. There was a clear relation between the anomalies on DRA δ and high electron fluxes observed for several days preceding the event. The electron fluxes from GOES and Meteosat-3 were used to calculate the fluence behind a thin foil (equivalent to a <1.5 mm Al). At the time of the anomalies the satellite had been exposed to a fluence above 10^{11} MeV cm^{-2}. This is enough to cause deep dielectric charging on the spacecraft. The local time of the anomalies, 6–12, also support this conclusion.

The results from Section 5.2 show that the anomalies on Meteosat-3 were associated with high fluxes at energies above 40 keV, indicating that many anomalies are caused by deep dielectric charging. There are also reasons to believe that the flux of electrons below 43 keV is increased, therefore deep dielectric charging is not necessarily the only possible cause. Also surface charging can cause some of the anomalies.

The deep dielectric charging is usually reported to occur in the sector 6–12 local time. The surface charging occurs mainly 22–08 local time. As concluded in Section 5.2. the anomalies that are not predicted are evenly distributed. The peak of the predicted anomalies occurs at 2–10 local time. In this sector both surface charging and deep-dielectric charging can take place. The local time pattern for surface charging during active periods was different (Wrenn and Sims, 1993). At quiet times, the anomalies are evenly distributed in local time. Non-predicted anomalies are randomly distributed (Table 5.14 rightmost column), indicating that cosmic rays might be a possible cause for these anomalies.

For Meteosat-3 the number of anomalies increased with time. The reason that the same result was obtained when the net was tested with different time periods may be that during the early days the high fluxes of electrons were not so frequent or of long duration and therefore less anomalies occurred. Deep-dielectric charging seems to be more commonly occuring during solar minimum. It would be interesting to study data from a satel-

lite launched during solar minimum and covering a solar maximum to compare the solar cycle effects with the ageing.

local time	12 point warning	predicted	not predicted	1 point warning	predicted	not predicted
22-24	489	93	**396**	51	17	**34**
0-2	435	91	344	50	18	32
2-4	**551**	**259**	292	**64**	**44**	**20**
4-6	556	195	361	61	35	26
6-8	509	148	361	60	30	30
8-10	526	184	342	62	30	32
10-12	393	83	310	44	12	32
12-14	336	**67**	269	34	**6**	28
14-16	**327**	82	**245**	**33**	12	21
16-18	342	68	274	37	9	28
18-20	348	80	268	35	7	28
20-22	367	81	286	39	11	28
average value	432	119	312	48	19	28

Table 5.14. Local time results from the analysis in Section 5.2. The threshold was set to 0.5. Therefore the success rate of the non-anomalies is not optimised to 80%, but higher. This gives the success rate of warnings only to approximately 30%. This table is only shown to identify the tendency of the forecast

5.5.1 Improved space environment monitors

In this study 50–60 % of the anomalies on Meteosat-3 and Tele-X have been predicted and associated with high electron fluxes. The possible cause of these high-energy particles is deep dielectric charging, but all of the predicted anomalies do not necessary have to be due to that. Electrons of low energies (below 30 keV) were not investigated and therefore anomalies caused by surface charging can have been missed. SEUs cannot easily be monitored and the percentages of anomalies due to SEUs is not established.

This study has used all anomalies that were available. When a new satellite is launched several anomalies occur which the operators have to understand. When they understand the behaviour of the satellite, only more pronounced anomalies that have an impact to the mission are reported. We recommend that all anomalies, also those without any impact on the mission, should be reported in order to understand the environmental influence on each spacecraft. Wrenn (1995) concluded “Comparison between ANIK and DRA δ might suggest that the higher the threshold, the fewer the discharges, but that when one does occur it will be larger and much more damaging; the chance of this happening increases with mission duration.”

Futher studies on anomalies associated with electron fluxes measured on spacecraft should take into account that:

- the time resolution has to be better than one day
- the number of input parameters should be kept low by pre-processing the data
- the natural variability of fluxes that a spacecraft encounters in orbit around the Earth can disturb the models so that the number of false alarms becomes high
- the analyzed data set must be big enough due to the large variability of the environment and in the cause of anomalies
- the model should be tested with a ”real” time-series of data.

The SREM instrument contains three particle detectors with high energy resolution, an internal dosimeter, and internal temperature measurement. This study shows that a high energy resolution of a space monitor is not needed. With an onboard monitor short time effects can be automatically used to give a warning. For post-event analyses and for onboard autonomous systems higher time resolution is preferred.

The SEU rates have mainly been monitored in LEO, and hence mainly the SAA and auroral oval effects are included. For an environmental monitor onboard a GEO spacecraft the long term variation of high energy particles are of interest. A long term investigation of SEUs on many spacecraft in GEO will give knowledge of the variations of cosmic rays and solar proton events. Since the Earth's magnetic field acts as a shield for cosmic rays, SEU detectors will be interesting to analyze. A SEU monitor is more or less a memory chip that holds a pattern in its memory cells. A computer continuously checks how many bit filps have occurred during the integration time and then resets the pattern. The memory cells that are selected for this type of monitor should be SEU sensitive but latchup resistant.

An environmental monitor for commercial satellites could also use the concept of Bogorad et al. (1995); a dosimeter measuring energetic particles from about 80 keV for internal charging and one or several detectors measuring the surface charging (can either be a dosimeter in the energy range about 1-30 keV or a plate detector). Measurements of the surface charge can, however give the information to late. The dosimeter measure accumulated total dose and might not have the temporal resolution needed for good forecast possibilities. In this study the influence of the electron above 2 MeV was not strong but we still believe that it is important to cover this energy range. In addition a sensitive memory chip to monitor the SEU rate is recommended. The impact of protons is not studied, but a dosimeter measuring the high-energy protons might help improving the understanding of the processes causing anomalies and to develop improved space weather monitors.

An environmental monitor must be able to survive the whole mission, although ground-based data can be used after the first part of the mission when the sensitivity to energetic particles is known. It is also shown that a fairly good forecast can be made using data from another spacecraft. There will, however, in the future also be other needs for a good knowledge about the space weather. A set of space weather monitors can

therefore play a very important role, in the same sense as meteorological instantaneous and long time series data are for the climatology today. Also the knowledge about the space "climate" will be essential when more space based tools are being used and more manned spacecraft are being launched. The weight and power consumption of an environmental monitor must be kept low.

5.5.2. Satellite anomaly index

If a spacecraft operator will use an index that predicts anomalies, it must be easy to use and reliable. A satellite can have no or numerous anomalies. Therefore the index needs to be flexible so the operator can adjust it after learning how the satellite behaves.

The forecast model can give a warning about 24 hours or less before the anomaly. The model is developed to correctly predict the non-anomalies with at least 80%. Using the energy flux directly is not recommended because the output of the model gives an index fluctuating between high and low almost at every point and the normal daily variation is clearly seen. The model that is easiest to read and have the largest difference between low and high is the model trained with anomalies associated with high fluxes. Therefore a satellite index we recommend indicates the presence of high fluxes in GEO. This index can be used on several spacecraft simultaneously.

The index can be used to find about 46% and 63% of the desired warnings, respectively. When the index is low, it is correct to 87% and 96%. The anomalies that the model does not predict are probably caused by other effects than high electron fluxes, i.e. this index is not built to predict them. The 23-24% of the time when the model have a high index it is to 36% to 22% true. If this is not accurate enough the threshold can be selected differently.

On the tested satellites the model predicted up to 70% of the anomalies. The model gives no warnings 75% of the time. Depending on the satellite sensitivity and selected threshold value, when the model gives a warning 22 to 36 % of the times is it correct.

5.6. Conclusions

All spacecraft are effected by the space environment, the difference is the threshold for the different interactions. The spacecraft designers must build the spacecraft to minimise the impact taking the available resources into account.

Operating the spacecraft tells the operator how each individual satellite behaves. After launch, the satellites often encounter many different anomalies both environmentally induced and others. When the satellite's behaviour is established, also harmless anomalies can be useful for further studies.

From the different forecast models one is selected as a good satellite index to warn satellite operators for time with high anomaly risk due to high fluxes of electrons. The forecast model warns if anomaly will occur within 24 hours. 75% of the time the model predicts low activity and low risk for anomalies. When the model warns for a high

anomaly risk within 24 hours, it is 22–36% correct depending on the spacecraft sensitivity.

High energy resolution is not needed for an environmental monitor capable of doing good forecasts. An environmental monitor can be a dosimeter, measuring in the energy interval between 40 keV and 10 MeV. The low-energy electrons (below 20 keV) were not studied here, but the low energies should be covered by an environment monitor to give a better understanding of spacecraft charging. SEU effects are also of interest but have mainly been studied in low Earth orbit.

Many satellites are equipped with environmental monitors to monitor the local environment. The instruments provide both information to the operator but also can be designed to warn autonomously. Many of the new monitors are still not tested in space.

Kp and Dst are good candidates for predicting anomalies and non-anomalies on GEO spacecraft, while electron flux (E > 2 Mev) is good for predicting anomalies and less good to predict non-anomalies.

Time-delay neural network and learning vector quantization network are well suited for the forecasting task. Both networks give similar forecast accuracy. Nevertheless, time-delay neural network gives a more stable performance than does learning vector quantization network.

With Kp as the input, using daily averaged data, the total forecast rate is about 80% at highest for events on Meteosat-3, the corresponding forecast rate for anomalies is 78% and for non-anomalies is 80%. And the total forecast rate is 64% for events on Tele-X, the forecast rate is 78% for anomalies and is 46% for non-anomalies. With Dst as the input, the total forecast rate is 73% at highest for events on Meteosat-3, the corresponding forecast rate for anomalies is 75% and for non-anomalies is 72%. And the total forecast rate is 64% for events on Tele-X, the forecast rate is 81% for anomalies and is 44% for non-anomalies. With electron flux (E > 2 MeV) as the input, the total forecast rate is 62% at highest for events on Meteosat-3, the corresponding forecast rate for anomalies is 86% and for non-anomalies is 35%. And the total forecast rate is 67% for events on Tele-X, the forecast rate is 93% for anomalies and is 36% for non-anomalies.

In order to describe the different local conditions in space environment for Meteosat and Tele-X, we investigated how the threshold value affects the forecast accuracy for anomalies and non-anomalies, for a given total forecast rate. By examining two trained neural network models, we have found a new threshold value for Tele-X which can give better accuracy of non-anomalies at the expense of accuracy for anomalies. In addition, the two network models show a similar variation of forecast accuracy with the threshold value. This indicates that the threshold value might be satellite-dependent and be associated with satellite local conditions (including local space environment, satellite design and materials, etc).